International Journal of Precision Engineering and Manufacturing-Green Technology (2021) 8:1347–1367
https://doi.org/10.1007/s40684-021-00337-4

Online ISSN 2198-0810
Print ISSN 2288-6206

REVIEW

Interfacial Solar Evaporator - Physical Principles and Fabrication Methods

Jungtaek Kim[1] · Jaewoo Hwang[1] · Seongheon Kim[1] · Seong Ho Cho[1] · Hanseul Choi[1] · Ho-Young Kim[1] · Yun Seog Lee[1,2,3]

Received: 13 February 2021 / Revised: 13 February 2021 / Accepted: 9 March 2021 / Published online: 5 May 2021
© Korean Society for Precision Engineering 2021

Abstract
Production of fresh water based on a renewable energy source is one of the most important global challenges for mankind due to ever-accelerating climate changes. Solar thermal evaporation shows promise for overcoming the water scarcity problem by utilizing solar energy, the most abundant and clean energy source. To enhance the performance of solar evaporators, interfacial solar evaporators have been introduced, which harness solar energy onto the water surface. To enable energy conversion and water evaporation at the interfaces of a solar evaporator, multi-scale heat and water transport have been investigated. Furthermore, various light-absorbing materials and system configurations have been studied to achieve the theoretical maximum performance. The fundamental physics of the interfacial solar evaporator, including thermal and water transport, and a broad range of interfacial solar evaporator devices in terms of the fabrication techniques and its structures are reviewed.

Keywords Solar evaporator · Photothermal · Evaporation · Capillary flow · Fabrication

1 Introduction

Water scarcity caused by climate change is one of the biggest global problems faced by mankind [1, 2]. Conventional technologies for water purification are mostly based on fossil fuels, resulting in environmental and sustainability issues [3]. To overcome the water scarcity problem, solar energy can provide as a sustainable solution owing to its abundance [4, 5]. Solar thermal distillation and desalination, which is one of the most conventional technologies utilizing solar energy directly, converts sunlight to thermal energy to evaporate water for purification, followed by the condensation process [6, 7]. It is environmentally benign, low-cost, electrically independent, and a decentralized system [8–10], which are important features for not only regions suffering from water shortages, but also for urban regions seeking water recycling. Solar thermal distillation can be considered as a miniature version of the water cycle of earth, in which water evaporates from the ocean by solar irradiance and condenses to clean water which is supplied to the ground by precipitation.

Among various types of solar thermal distillation, a solar still has been the most feasible system to produce fresh water with its simple equipment setup. A solar still consists of two reservoirs in a transparent case: one is a bath of water to be evaporated and the other is a container collecting the condensed water. Water vapor is cooled by the ambient air, and the condensed water droplets slide along the inclined condensing plate and are accumulated in the container. Although solar stills have been used for a long time, inefficient sunlight absorption has limited its solar energy utilization and throughput of clean water production (Fig. 1a). Pure water cannot absorb the solar spectrum (280–2700 nm) effectively, except for infra-red which is easily absorbed by a thin water layer (~0.1 m) [11]. Additionally, light absorption occurs through the bulk water in a reservoir and the reservoir wall, resulting

Invited Review: This paper is an invited paper.

✉ Ho-Young Kim
hyk@snu.ac.kr

✉ Yun Seog Lee
leeyunseog@snu.ac.kr

[1] Department of Mechanical Engineering, Seoul National University, Seoul 08826, Republic of Korea

[2] Institute of Advanced Machines and Design, Seoul National University, Seoul 08826, Republic of Korea

[3] Inter-University Semiconductor Research Center, Seoul National University, Seoul 08826, Republic of Korea

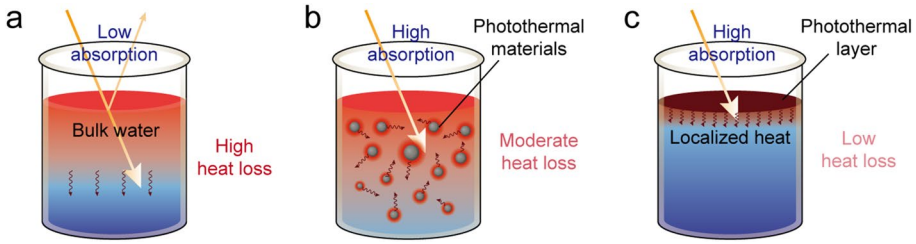

Fig. 1 Three types of solar-driven evaporators. **a** Solar still. **b** Bulk heating with light-absorbing particles. **c** Interfacial solar evaporator. Blue and red colors indicate cold and hot regions, respectively (color figure online)

in a volumetric heating. However, water evaporation can only occur on the surface of the water. Heat is easily dissipated to the reservoir wall and not directly utilized in evaporation. To enhance the sunlight absorption, a strategy of including light absorbing particles in water has been employed (Fig. 1b) [12–14]. However, as described above, bulk heating methods still suffer from a heat loss issue with the generated heat inefficiently utilized for evaporation.

To resolve the heat loss issue, an interfacial solar evaporator has been investigated. Sunlight is absorbed at the water–air interface by introducing a capillary-driven water evaporation panel (Fig. 1c). The first interfacial solar evaporator consists of hydrophilic porous media which can absorb the full spectrum of sunlight and passively imbibe water while it floats on the surface of the water [15, 16]. However, a significant portion of the heat generated from the light absorber was lost to the bulk water. Therefore, a modified structure with an additional insulating layer underneath has been employed [17]. Furthermore, various materials, system configurations, and manufacturing methods for the interfacial solar evaporator have been extensively investigated for a higher conversion efficiency and evaporation rate.

In this review, the physical principles of an interfacial solar evaporator are introduced in terms of the thermal and fluid transport processes. Then, various manufacturing methods for the interfacial solar evaporator devices and their strengths and weaknesses are discussed. Finally, further research directions and novel concepts are discussed.

2 Thermal Principles—Photothermal Conversion

2.1 Photothermal Conversion

For solar evaporation, a photothermal energy conversion process of sunlight into heat energy must occur first. The converted thermal energy needs to be utilized efficiently for the liquid–vapor phase change of the water (Fig. 2). We begin our discussion with the photothermal effect.

Solar radiation energy in the form of electromagnetic waves travels through the Earth's atmosphere, and only a limited wavelength range (UV–VIS–NIR) can reach the soil and be harnessed for solar energy applications (Fig. 3a). Here, UV, VIS, and NIR stand for ultraviolet, visible, and near-infrared, respectively. When the sunlight reaches the surface of objects, it is transmitted, reflected, and absorbed, and their relative amount is respectively denoted as transmittance (T), reflectance (R), and absorptance (A). The transmittance of solar absorbing material needs to be 0, to enhance the absorption for heat utilization. From the ratio of the absorbed light energy (I_{ab}) and the total solar flux over the solar spectrum, the averaged optical absorptance ($\overline{\alpha}$) can be defined as follows:

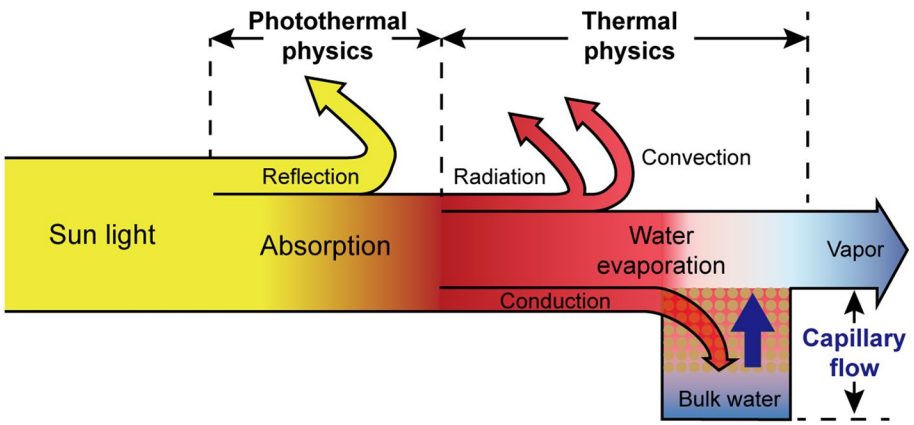

Fig. 2 Schematic diagram of solar thermal evaporation with governing physical principles

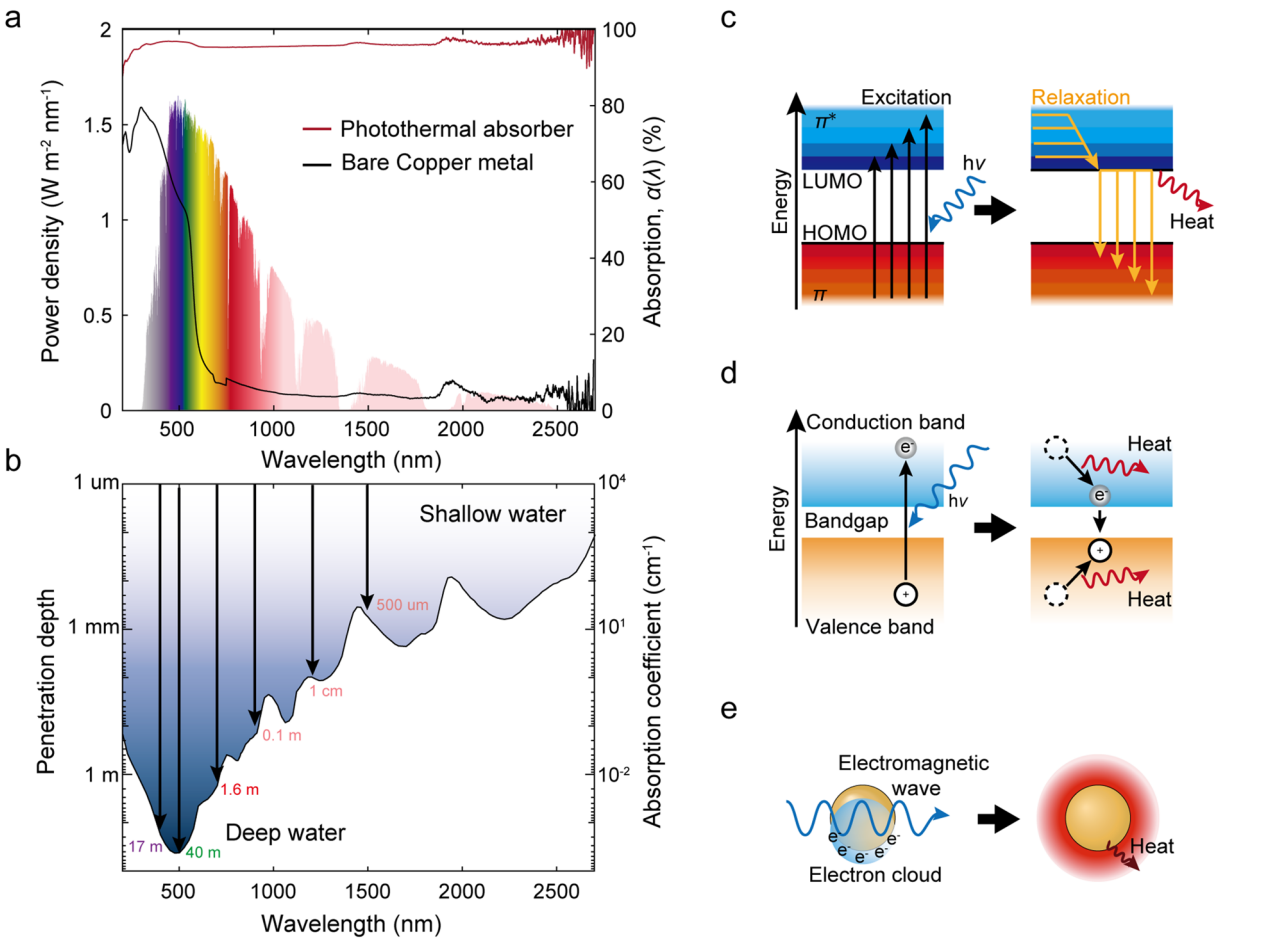

Fig. 3 Photothermal principles and various photothermal mechanisms. **a** Solar spectrum and absorption rate. **b** Light penetration depth in water. **c** Thermal vibration of molecules. **d** Electron–hole generation and relaxation. **e** Plasmonic heating

$$\overline{\alpha} = \frac{I_{ab}}{I_T}, I_{ab} = \int_{280nm}^{2700nm} I_{solar}(\lambda) \cdot \alpha(\lambda) d\lambda,$$

$$I_T = \int_{280nm}^{2700nm} I_{solar}(\lambda) d\lambda.$$

where $I(\lambda)$ is the AM1.5G spectral solar irradiation intensity over a wavelength (λ) range from 280 to 2700 nm. Because the irradiated solar energy per unit area is fixed, the higher light absorption is necessary for better evaporation performance of the interfacial solar evaporator. Due to the low absorptance of bulk water (Fig. 3b) [11], many studies have been conducted to develop novel materials with high absorptance, referred to as photothermal materials.

2.2 Photothermal Materials

Photothermal conversion is a process in which a substance is excited by light and releases heat while it returns to its initial energy state. It involves three principles: (1) thermal vibration of molecules (Fig. 3c), (2) electron–hole generation and relaxation (Fig. 3d), and (3) plasmonic heating (Fig. 3e). The typical photothermal materials are (1) carbonaceous and polymeric materials, (2) metal oxide-based semiconductors, and (3) plasmonic metal nanoparticles.

2.2.1 Carbonaceous and Polymeric Materials

Carbon materials and many polymers have abundant electrons that exist loosely in the π-orbital while carbon atoms bond with the sp^2-orbital [18]. These electrons in π-orbital are excited to a higher energy state by photons with the corresponding energy difference, moved from the lower energy state (highest occupied molecular orbital, HOMO) to the higher energy state (lowest unoccupied molecular orbital, LUMO), π^*-orbital. They emit thermal energy during relaxation to the initial energy state (Fig. 3c) [19].

Carbonaceous materials are widely used in solar evaporators in the form of amorphous carbon, graphene, graphite

oxide, carbon nanotubes, graphite, or carbon black, demonstrating excellent absorption in a broad solar spectra and having the potential of cost-effective large-scale fabrication processes. In addition, some special polymer materials, such as polypyrrole (PPy) [20, 21] and polydopamine [22], have also been used in high-efficiency solar evaporators recently.

2.2.2 Metal Oxide-Based Semiconductors

Semiconductor materials generate electron–hole pairs by absorbing photons with energy higher than their bandgap. The electrons and holes move to the conduction and valence band, respectively, and generate heat as they relax to the edge of the band or lead to non-radiative recombination. The rest of the energy is emitted during the radiative recombination (Fig. 3d) [23, 24]. For efficient photothermal conversion, a narrow band gap is necessary to increase the range of the photon energy to absorb and reduce the energy loss by emission. Therefore, some studies were aimed to reduce the bandgap through doping or synthesizing cost-effective materials with an ultra-low bandgap.

Various metal oxides with narrow bandgaps have attracted much attention as photothermal materials due to low material-cost and accessible synthesis. In particular, titanium-based materials including TiO_X (black titania) and Ti_2O_3 have high absorbance for sunlight [25–29]. Various metal oxides such as AlO_3 [30], CuS [31–33], and MoO_3 [34] also have been introduced and shown to be applicable in high-efficiency solar evaporators.

2.2.3 Plasmonic Metal Nanoparticles

Some noble metal elements including Au and Ag have an excellent ability to absorb light and convert it into heat, due to their plasmon resonance [35]. Vibration occurs when the natural frequency of electrons on the metal surface matches the frequency of light, and then heat is released to the surroundings during relaxation (Fig. 3e). Due to these characteristics, various plasmonic materials (including Au nanoparticles) have been spotlighted as a novel class of light absorbing materials for solar evaporators. However, it has been difficult to absorb a broad spectrum of sunlight because the specific size of the plasmonic particles can only absorb light in a narrow band (*e.g.* 400–800 nm for 18-nm-large Au nanoparticle) [16]. To overcome the light selectivity, self-assembled nanoparticles were introduced to prepare a broad size distribution of nanoparticles, which can absorb a wider range of wavelengths of sunlight (400–2500 nm) [36]. Through this strategy, various solar evaporators with plasmonic nanoparticles achieving considerable efficiency have been studied. However, the cost of noble metal is considered an obstacle.

3 Thermal Principle—Heat Utilization

Previous studies on interfacial solar evaporators with a variety of materials and structures have focused on achieving the ideal conversion of the limited solar radiance into evaporation. Converting the entire solar radiance to evaporation is virtually impossible because the temperature gradient inevitably increases the heat losses to the atmosphere and surrounding systems by conduction, convection, and radiation. To reduce these heat losses and enhance the utilization of energy into water evaporation, diverse methods have been presented by considering both the materials and structure.

We first investigate the fundamentals of thermal transport by the mass-energy balance of a solar evaporator. The inflow and outflow of water and thermal energy are modeled. Then, the evaporation on solar evaporator is quantified by physical relationships. Subsequently, we introduce various methods for enhancing evaporation performance in terms of the heat transfer. Lastly, we present general mathematical models for 1D and 2D structures, which can be employed to design interfacial solar evaporators and examine their performances.

3.1 Mass and Heat Balance

The mass-energy balance scheme for an interfacial evaporator is shown in Fig. 4a. Due to the capillary pressure, water (mass) ascends from the reservoir through the solar evaporator and evaporates at the surface in contact with the ambient air. In contrast to the one-way route of the mass transfer mechanism, heat transfer is much more complicated. While the solar radiance absorbed at the surface is the only source of heat energy, it leaves the evaporator via four different routes: conduction to the water reservoir, evaporation in the form of vapor, convection to the adjacent air, and radiation to the whole surroundings. Among these, passages other than evaporation can be considered as heat-loss. Two physical assumptions have been made in the model. Firstly, we only concentrate on the steady-state effect; thus, the net value of the mass and energy storage in the evaporator should be zero. Secondly, because most of the interfacial evaporators are flat, we can neglect the mass- and energy-transfers arising at the side of the evaporator.

Water and thermal energy transports occur in the opposite direction at the bottom of the evaporator touching the water. Water is supplied into the evaporator due to the capillary pressure. At the same time, heat transfers in the form of conduction due to the higher temperature of the

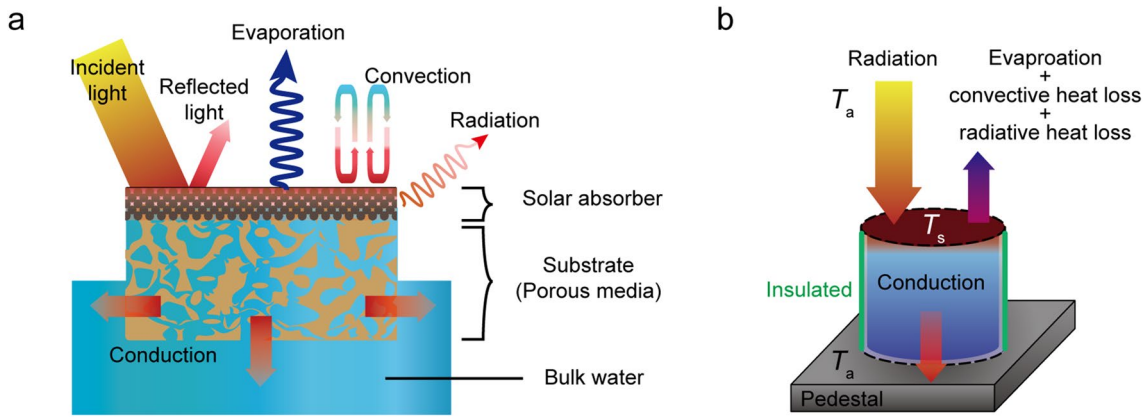

Fig. 4 Heat utilization of interfacial solar evaporators. **a** Mass and energy balance scheme. In contrast to the one-way passage of mass transfer, heat transfer has more sophisticated byways. **b** Schematic illustration for a simplified model for interfacial solar evaporator

evaporator than the static water reservoir. Because the rate of mass transport by the capillary flow is much slower than the conductive heat transfer, the effect of heat carried by the fluid flow can be neglected. At the top of the evaporator, heat transfer occurs in a more complex fashion. The solar irradiance is absorbed on the surface; and the water with a significant portion of the thermal energy exit simultaneously in the form of evaporation. The rest of the thermal energy is discharged in the form of convection and radiation.

Evaporation occurs due to the concentration gradient between the water surface and air, where the interfacial vapor is locally equilibrated with the liquid water [37]. The elevated temperature of the evaporator results in a higher vapor concentration on the surface [38], thus accelerating evaporation. Convective heat transfer by natural convection takes place at the top of the evaporator surface. The temperature difference between the ambient and evaporator surface also results in net radiative heat loss.

3.2 Physical Principles

Renowned relationships clarify conduction (Fourier's law) and radiation (Stefan–Boltzmann law). Convection, based on the flow type (natural convection or forced convection) and geometry, can be quantified by theoretical [39, 40] or experimental [41, 42] methods. Heat and mass transfer via evaporation has been modeled in previous literatures [37, 43, 44]. However, a comprehensive model simultaneously incorporating natural convection, latent heat transfer, and temperature dependent concentration change needs to be further developed.

Unlike other heat transfer mechanisms where the sensible heat flows out into the surrounding system, the evaporative heat is used in the phase transition of water. Therefore, the evaporative heat can be represented as the product of vaporization enthalpy (h_{fg}) and the evaporative mass transfer rate.

$$Q_{\text{evap}} = h_{fg}\dot{m}. \tag{1}$$

The mass transfer rate can be represented as the product of the mass transfer coefficient (h_{mass}), partial pressure difference between surface and ambient air ($p - p_0$), and area

$$\dot{m} = h_{\text{mass}}(p - p_0)A. \tag{2}$$

By substituting Eqs. (2) into (1), the evaporative heat flux can be written as

$$Q_{\text{evap}} = h_{fg}h_{\text{mass}}(p - p_0)A. \tag{3}$$

The mass transfer coefficient can be obtained by analytical [45], numerical [43], or experimental methods [44]. Among the relations between heat and mass transfer proposed in various studies, we adopted the relation for water deduced by Bowen [45]:

$$Q_{\text{conv}}/Q_{\text{evap}} = 0.46\frac{\Delta T}{\Delta P}, \tag{4}$$

where ΔT is the temperature difference between water surface and temperature in the unit of Kelvin, and ΔP is the partial pressure difference between the water surface and temperature in the unit of mmHg. To describe the relationship solely in terms of temperature, the Antoine equation [38] is used,

$$Q_{\text{conv}}/Q_{\text{evap}} = 0.46 \times \frac{\Delta T}{10^{8.07-\frac{1730}{T[K]-40}} - \frac{p_0}{133.322}}, \tag{5}$$

where p_0 is the partial pressure of the vapor in ambient air, in the unit of Pascal. Finally, the evaporative heat flux can be written as

$$Q_{\text{evap}} = \dot{m}h_{fg} = \int_{S_a} 2.17 \times h \times \left(10^{8.07-\frac{1730}{T[K]-40}} - \frac{p_0}{133.322}\right) dA. \tag{6}$$

The efficiency for solar evaporator is the ratio of the total energy used in vaporization to the total incident solar radiance:

$$\eta = \frac{Q_{\text{evap}}}{I_{\text{incident}}}. \tag{7}$$

3.3 Strategies to Enhance Evaporation

Previous studies have introduced diverse strategies to enhance the performances of solar evaporator devices, which can be sorted into three categories: insulation addition (1D, 2D), evaporation area increment (3D), and vaporization enthalpy reduction. These strategies and some archetypes of each category have been classified as the following.

3.3.1 Insulation Addition (1D, 2D)

Elevated temperature in the evaporator results in adverse effects on its performance. Increased temperature at the top of a solar evaporator facilitates evaporation of the surficial water. However, the increased temperature also promotes heat losses: the increased temperature difference between the bottom of the solar evaporator and the static water reservoir results in a higher heat loss by conduction. An increased temperature difference between the top of the solar evaporator and ambient air results in a higher convective loss and the radiative loss. While evaporation, convection, and radiation depend on the temperature of top part of the evaporator, the conductive heat loss depends on the temperature of the bottom part of the evaporator. Experiments and numerical calculations [46] indicate that conductive heat loss to the water reservoir accounts for the largest heat loss, followed by convective heat loss to the air and radiative heat loss to the surroundings. Convective heat loss generally has a positive relationship with the evaporation, therefore suppressing convective heat loss may give negative effects on the efficiency. Radiative heat loss is negligible under 1-Sun irradiation; thus, its suppression would be less worthwhile.

Adding insulation between the water and the evaporator has been a straightforward method to lower the temperature of the bulk water-evaporator interface while maintaining the temperature of the top surface. Ghasemi et al. first presented an interfacial evaporator with insulation between the water and the evaporator [15]. Compared to the relatively high thermal conductivity of the evaporator (0.959 W m^{-1} K^{-1}), the insulation had a low thermal conductivity of 0.426 W m^{-1} K^{-1}. The insulation device localized the high temperature at the top by blocking the thermal conduction to the water reservoir, increasing the efficiency from 55 to 65% under a 1-Sun condition.

The thermal conductivity of insulation devices cannot differ much from the thermal conductivity of water (0.6 W m^{-1} K^{-1} at 20 °C), because water imbibed in the insulation devices is also incorporated in heat conduction. Li et al. suggested a solar evaporator with two-dimensional water pathway by placing a polystyrene foam as a water impermeable insulator at the center [17]. The low thermal conductivity of the polystyrene foam (0.04 W m^{-1} K^{-1}) enabled a high efficiency of 85% under a 1-Sun condition. Yu et al. lifted the evaporation device from the water by using capillary channels as pillars, so that the extremely low thermal conductivity of air (0.02 W m^{-1} K^{-1}) could be exploited [47]. Air worked as an impressive insulator, raising the device efficiency as high as 98.1% under a 1-Sun condition.

3.3.2 Evaporation Area Increment (3D)

As Eq. (3) implies, the evaporation rate corresponds to the product of the mass transfer coefficient, concentration difference, and evaporation area. 1D and 2D evaporation devices focus on maximizing the concentration difference by maximizing the surface temperature. In contrast, some studies are concerned with increasing the evaporation area by constructing 3D structures. For example, Li et al. suggested a 3D solar evaporation device with vertical hollow columns [48]. The temperature of the top surface was only 26.6 °C under a 1-Sun condition, but they reached a solar energy efficiency over 100%. This over-perfect efficiency is because of the intrinsic evaporation due to the original concentration difference between the evaporator surface and the air. Singh et al. proposed an inclined solar evaporator with open-capillary structure [49]. By adjusting the angle of inclination, the positive effect of the evaporation area increment has been demonstrated on the efficiency. However, the addition of area does not always increase the evaporation rate because the limited solar radiance is deconcentrated on the broad surface and lowers the temperature. Therefore, when designing a 3D solar evaporator, it should be ensured that the effect of the increased area dominates the effect of the lowered temperature.

3.3.3 Vaporization Enthalpy Reduction

Bulk water has a vaporization enthalpy of 2454 kJ/kg at 20 °C. The high vaporization enthalpy is because the strong hydrogen bonds of every single water molecule should be separated when evaporating. However, when water molecules near surface are in a specific interaction with a

substrate, the water molecules are expected to form a cluster of 2–10 water molecules [50, 51]. In contrast to the case where each water molecule evaporates independently by cutting every hydrogen bonds, evaporation of clustered water molecules needs a smaller vaporization enthalpy because cutting the exterior hydrogen bonds of the water cluster is sufficient. Nano- and micro-structures enabling such water clusters have been proposed by using various materials. Zhao et al. [52] reported a reduced vaporization enthalpy of 1555 kJ/kg by fabricating $Zr(Ti)O_3$ nanotube arrays with a pore size of 50 nm on the evaporator surface. Guan et al. reported a vaporization enthalpy of 997 kJ/kg with a bacterial cellulose nanocomposite with cross-linked carbon nanotube nanostructures [53]. By using hydrogel as the material for the evaporator, Zhao et al. reported a vaporization enthalpy of 1300 kJ/kg [54]. Zhou et al. developed a method to tune the vaporization enthalpy by adding chitosan into light-absorbing hydrogel [55]. The hydrophilic functional groups (hydroxyl and amino groups) of chitosan strongly interacted with the water molecules, decreasing the vaporization enthalpy to 881 kJ/kg.

3.4 Theoretical Model for Interfacial Solar Evaporators

3.4.1 Assumptions and Settings

Only a few of the previous studies on interfacial solar evaporators modeled their works with rigorous consideration of the heat transfer. Ghasemi et al. assumed convection coefficient of 5 W m^{-2} K^{-1}, and determined the evaporative heat transfer coefficient as 120 W m^{-2} K^{-1} by measuring the vapor temperature [15]. Numerical simulation was conducted using COMSOL based on those values. In the work by Ni et al. where an innovative method to generate solar steam by a geometric thermal concentration was presented, the measured value of the experimental evaporation rate (200 W m^{-2} K^{-1} at 40 °C) was used when implementing the model in the COMSOL simulation [56]. In another work from Ni et al. where they presented an analytical model demonstrating volumetric solar heating by nanoparticles, they fitted the evaporation rate computed by COMSOL (150 W m^{-2} K^{-1}) in their analytical model [13]. However, to the best of our knowledge, a generalized mathematical model for an interfacial solar evaporator has not been presented that incorporates the coupled effect of evaporation, natural convection, and surface temperature. In this part, we present our original mathematical models for quantitative analysis of 1D and 2D interfacial solar evaporators by incorporating the physics provided in the previous part into an ordinary differential equation with the appropriate boundary conditions. For 3D interfacial evaporators, different natural convection models should be used depending on the specific geometry of solar evaporator.

We modeled the general experimental setup as depicted in Fig. 4b. Studies on 1D and 2D interfacial solar evaporators have wide length scales ranging from millimetric to centimetric scales. The size and shape may affect the performance of the evaporator [57, 58], but we adopted a uniform shape for a simple model. The model resembles the experimental setup made by Ghasami et al., where a 10-mm-thick evaporator was placed on a cylindrical chamber with the inner diameter of 50 mm and a height of 96 mm, and the sidewall was insulated by aerogels [15]. When insulation was added in the mathematical model, we adopted the practice of Ghasami et al. by placing a 5-mm-thick insulation layer between the water and the evaporator.

3.4.2 Governing Equation and Boundary Conditions

The general governing equation for heat transfer in all domains is deduced by combining the differential energy balance equation with Fourier's law, as follows:

$$\rho c_p \frac{\partial T}{\partial t} + \rho c_p \underline{v} \cdot \nabla T = k\nabla^2 T + \dot{q} + \Phi, \tag{8}$$

where $\underline{v}$ is the velocity of water; $\dot{q}$ is the internal heat generation, and Φ is the viscous energy dissipation represented as the double dot product of the shear stress tensor and rate of deformation tensor ($\tau : D$). We only concentrated on the steady state behavior, so the time derivative term can be eliminated. The surface of the interfacial solar evaporator absorbs all the solar radiance, thus the heat generation term in all domains is zero:

$$\rho c_p \underline{v} \cdot \nabla T = k\nabla^2 T + \Phi.$$

In the water domain, natural convection hardly occurs because it is hotter at the upper part contacting the evaporator, and cooler at the lower part contacting the pedestal [59]. Therefore, the terms related to velocity are vanished, leaving the pure conduction term as the governing equation as follows:

$$k_w \nabla^2 T = 0, \tag{9}$$

where k_w is the thermal conductivity of water.

In the porous evaporator and insulator, water drawn by capillary forces flows along the evaporator. Based on the flow rate, the velocity of the water typically is on the order of 10^{-5} m/s [54]. Comparing the orders of the velocity-related terms to the thermal conduction terms, the convective term ($\rho c_p \underline{v} \cdot \nabla T$) and dissipative term ($\Phi$) may be neglected. Therefore, the porous evaporator and insulator are also governed by the pure conduction equation as follows:

$$k_p \nabla^2 T = 0, \tag{10}$$

where k_p is the thermal conductivity of the porous evaporator or insulator imbibing water. The thermal conductivity of the porous structures imbibing water can be estimated if the thermal conductivity and porosity of the unwetted structure are known [60, 61]. The same governing equation is applicable for hydrogel evaporators because the speed of water diffusion in hydrogel is very slow compared to the thermal conduction [62]. When the hydrogel is in a swollen state, the thermal conductivity of the hydrogel may be regarded as the thermal conductivity of water because the swollen hydrogel predominantly consists of water [63].

Figure 4b shows the boundary conditions applied. The table (pedestal) upholding the cylindrical apparatus is assumed to be much bigger than the beaker and very conductive, so that the bottom temperature of the water might be assumed equal to the ambient temperature. The side of the beaker is set as insulated. At the top of the beaker, the combined effect of solar radiance, evaporation, convection, and radiation should be set as the boundary condition. The net outward heat flux can be represented as follows:

$$\begin{aligned} q''_{\text{net}}(T_s) &= h(T_s) \times (T_s - T_a) + 2.17 \times h(T_s) \\ &\times \left(10^{8.07-\frac{1730}{T_s-40}} - 0.5 \times 10^{8.07-\frac{1730}{T_a-40}}\right) \\ &+ \varepsilon\sigma\left(T_s^4 - T_a^4\right) - \alpha q_{\text{sun}}, \end{aligned} \tag{11}$$

where T_s and T_a are the surface and atmosphere temperatures, respectively. The temperature dependent convective heat transfer coefficient $h(T_s)$ can be obtained from experiments. The experimental data obtained by Hassani et al. lead to [57, 64]:

$$h(T_s) = 2.91 \times (T_s - T_a)^{0.194}. \tag{12}$$

3.4.3 1D Solar Evaporator Model

A one-dimensional solar evaporator can be modeled by two domains serially in touch with each other. Both the water and evaporator domains are governed by the conduction equation with the thermal conductivity of the water or evaporator. The boundary condition at the bottom is set as ambient temperature (Dirichlet boundary condition), and at the top, the combined effect of solar radiance, evaporation, convection, and radiation is set as the boundary condition (Neumann boundary condition):

$$k \nabla^2 T = 0$$

$$k = \begin{cases} k_w & 0 \le z \le H_w \\ k_e & H_w \le z \le H_w + H_e \end{cases}$$

$$T(z = 0) = T_a$$

$$k_e \frac{dT}{dz}(z = H) = q''_{\text{net}}(T_s).$$

Because the Laplace equations in two domains yield two linear temperature profiles, algebraic manipulations are sufficient to deduce the equation for the surface temperature. The calculations yield the following implicit relationship:

$$T_s - T_a + \left(\frac{H_w}{k_w} + \frac{H_e}{k_e}\right) q''(T_s) = 0. \tag{13}$$

If insulations are added, an extra domain with the thermal conductivity of the insulator is added:

$$k = \begin{cases} k_w & 0 \le z \le H_w \\ k_{in} & H_w \le z \le H_w + H_{in} \\ k_e & H_w + H_{in} \le z \le H_w + H_{in} + H_e \end{cases}.$$

Solving the system of equations with the same boundary conditions as above, a new implicit equation can be obtained as follows:

$$T_s - T_a + \left(\frac{H_w}{k_w} + \frac{H_i}{k_i} + \frac{H_e}{k_e}\right) q''(T_s) = 0, \tag{14}$$

where the index i represents the insulation.

3.4.4 2D Solar Evaporator Model

A two-dimensional solar evaporator is essentially an insulation-added one-dimensional evaporator with additional water pathways. The effect of the water pathways on the thermal conductivity can be incorporated by parallel conduction analysis as follows [65]:

$$k_{par} = k_p A_p + k_{in} A_{in}, \tag{15}$$

where A_p is the areal ratio of the porous water pathway, and A_{in} is the areal ratio of the insulation. The insulation can be either a solid [17] or air [47]. The relationship for 2D evaporators is identical to what has been deduced by the 1D evaporator with insulation added, but the thermal conductivity of the insulation should be replaced by k_{par}:

$$T_s - T_a + \left(\frac{H_w}{k_w} + \frac{H_i}{k_{par}} + \frac{H_e}{k_e}\right) q''(T_s) = 0. \tag{16}$$

4 Fluid Dynamics—Capillary Limit

The interfacial solar evaporator isolates the water in a solid matrix, a porous medium, from the bulk water to achieve interfacial heating. While the vapor is generated at the liquid–air interface over the porous matrix, water is replenished by capillarity from the bulk water. This passive pumping, capillary flow is driven by the difference between the pressure below the liquid–air interface, $p_i = p_a - \gamma\kappa$, and the atmospheric pressure, p_a, where γ and κ are the surface tension coefficient and the curvature of the interface, respectively. This pressure jump is called the Laplace pressure which can be scaled as $\sim \gamma/r_p$, estimating the radius of the curvature of the meniscus as the radius of the pore conduit, r_p. In porous media, the fluid flow is described by Darcy's law as follows:

$$q = -\frac{K}{\mu}\nabla p, \tag{17}$$

where q is the volume flux and ∇p is the pressure gradient. The permeability K is proportional to the cross-sectional area of the fluid path and quantifies how easily liquids can flow through a porous matrix. By applying Darcy's law to the capillary flow with a sharp wetting front, the volume flux of the porous media, q, is scaled as $\sim \gamma K/(\mu r_p l)$, where l is the distance from the bulk water surface to the top surface of the porous media where evaporation occurs. Here, we classify the interfacial solar evaporator into 3 types (1D, 2D and 3D) corresponding to the limiting aspect of the capillary flow.

When the evaporation area is equal to the cross-sectional area of the porous media in which the capillary flow occurs, we define the system as 1D-interfacial solar evaporator system (Fig. 5a) which includes several interfacial solar evaporator studies in the early stage. The operation limit of a 1D system can be defined as $q > q_e$, that is, K is large enough or r_p is small enough to compensate for the evaporative flux, q_e, without dry-out owing to sufficient capillary flow rate.

To reduce parasitic heat loss, anisotropic porous media, which have a directional conduit, are employed to provide single or bundle of paths of liquid to the upper solar absorbing layer (Fig. 5b). These paths with high permeability, calculated as $R^2/8$, where R ($>> r_p$) is the radius of the conduit, compensate for the evaporation flux in absorbing layer and the thermal insulation.

3D structured solar evaporators with an efficiency over 100% have been reported. These 3D macro-structured solar evaporators suffer from the dry-out issue because the capillary flow is limited by the gravitational force and evaporation loss. Therefore, unlike a planar solar evaporator with moderate design limit, it is essential to predict the wet length of the 3D structure. These structures can be simplified as a porous medium standing perpendicular to the water surface like a fin structure.

When gravity can be neglected, we can derive a simple scaling law for the maximum wetting length, l_{max} under evaporation based on mass conservation. The inflow rate per unit width through the porous media, Q_{in}, and the outflow rate unit width through the liquid–air interface by evaporation, Q_{out}, can be described as follows:

$$Q_{in} = \tau_p\left(\frac{K}{\mu}\frac{2\gamma}{r_p l_{max}}\right)$$

$$Q_{out} = l_{max} q_e,$$

where τ_p is the thickness of the porous media, and q_e is the evaporation flux through liquid–air. The evaporation at the thickness side can be neglected assuming the thickness to be much smaller than the width. By equating Q_{in} and Q_{out}, we can estimate the wetting length as follows:

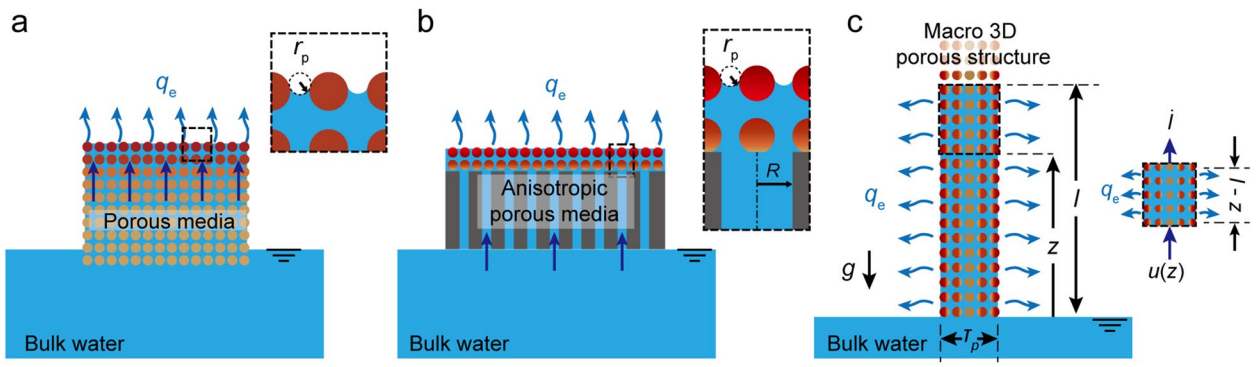

Fig. 5 Type of interfacial solar evaporators categorized by fluid transport. **a** 1D type with porous media. **b** 2D type with anisotropic pore structure. **c** 3D type with evaporation area increment

$$l_{\max} \sim \sqrt{\frac{\gamma K \tau_p}{\mu r_{\mathrm{P}} q_{\mathrm{e}}}}.$$

When both the gravity and evaporation effect are important, the capillary rise height is much more restricted. In a similar way we can model the flow velocity through the porous media by balancing the in–out flow rates based on mass conservation as follows (Fig. 5c):

$$u(z) = \dot{l} + \frac{q_{\mathrm{e}} l}{\tau_p}\left(1 - \frac{z}{l}\right). \tag{18}$$

Here, z is the elevation from the bulk liquid surface. The capillary rise in the porous media can be modeled by Darcy's law as follows:

$$u(z) = -\frac{K}{\mu}\frac{\partial(p + \rho g z)}{\partial z}.$$

To obtain the pressure balance between the driving pressure and the pressure drop by gravity and evaporation, we integrate the equation above with respect to z from 0 to l after substituting the equation from mass conservation, Eq. (18). Then a differential equation for the wet length is obtained as follows:

$$\dot{l} = \frac{a}{l} - b - cl,$$

where $a = 2\gamma K/(r_{\mathrm{p}}\mu)$, $b = \rho g/\mu$, $c = q_{\mathrm{e}}/(2\tau_p)$.

Because the maximum wet length corresponds to the moment when the liquid rise stops, $\dot{l} = 0$, $l_{\max}$ is algebraically given as follows:

$$l_{\max} = -\frac{\rho g \tau_p}{\mu q_{\mathrm{e}}} + \sqrt{\left(\frac{\rho g \tau_p}{\mu q_{\mathrm{e}}}\right)^2 + \frac{4\gamma K \tau_p}{\mu r_p q_{\mathrm{e}}}}.$$

Through this analytical modeling for capillary flow, it is possible to design the size limit of various forms of interfacial solar evaporators. In particular, an optimal conduit design can be attempted to prevent dry-out, which is more severe in scaled-up systems.

5 Fabrication of Interfacial Solar Evaporators

The key characteristics of an interfacial solar evaporator for efficient evaporation are a high photothermal conversion and focused heat on the surface of the water. Therefore, the fabrication methodology for an interfacial solar evaporator mainly consists of choosing the photothermal material and system configuration for heat utilization. Early research focused on new photothermal materials which are placed on the water surface. Afterwards, to improve the efficiency, a structure that does not directly contact the water surface was selected, while a floating object and capillary path did contact the water surface. Recently, to achieve further efficiency, various approaches have been attempted to fabricate 3D interfacial solar evaporators that can re-absorb light or collect ambient thermal energy. Here, we review the materials and manufacturing methods according to the system dimension classification.

5.1 1D Interfacial Solar Evaporators

The initial concept of an interfacial solar evaporator consisted solely of an evaporating surface floating on the water [15, 16, 31, 66–68]. By mimicking a porous biological evaporative surface, nanometer-size solar absorbers were uniformly dispersed on the surface of the bulk water. In this method, floatable solar absorbers were investigated to increase the solar absorption of the absorber materials to enhance the photothermal conversion efficiency. Carbon foam supported by exfoliated graphite [15], Fe_3O_4/carbon nanoparticles [66], hollow carbon-beads [67], and Au nanoparticles [16] were investigated as floatable solar absorbers (Fig. 6a).

Solar absorber materials need to be floatable and water permeable. To use a broader range of solar absorbers were modified to have a porous sponge-like floatable structure [25, 69–74]. Figure 6b shows an example of a fabricated solar absorber with a porous structure [69]. A hybrid hydrogel was formed by reduced graphene oxide with the aid of a cross-linking agent. The hybrid hydrophilic polymer framework and solar absorber efficiently transported water by capillary pumping and osmotic swelling with high water evaporation rate of 2.5 kg m^{-2} h^{-1} under a 1-Sun illumination (Fig. 6b). Hot compression molding was adopted to fabricate a sponge-like structure, such as a black polyurethane sponge [70] and carbon pencil shavings (CPS) [71].

However, the devices with porous evaporative surfaces have shown low evaporation rate (0.83–1.13 kg m^{-2} h^{-1} under 1-Sun illumination) [25, 70, 73], which are significantly lower than the theoretical value, mostly due to inefficient water transport and the limitations of the low-density solar absorber material. Therefore, a new concept for a solar evaporator based on hybrid materials has been introduced, where light absorption and water transport functions were implemented by different materials and structures. A highly efficient light absorber layer was combined with a water transport layer, which is typically a porous floating membrane. Therefore, the two requirements of high light absorption and efficient water transport could be satisfied [26–29, 32, 34, 56, 75–93]. Light absorbers were either mixed with a structure material to form a hybrid or deposited on the existing water transport

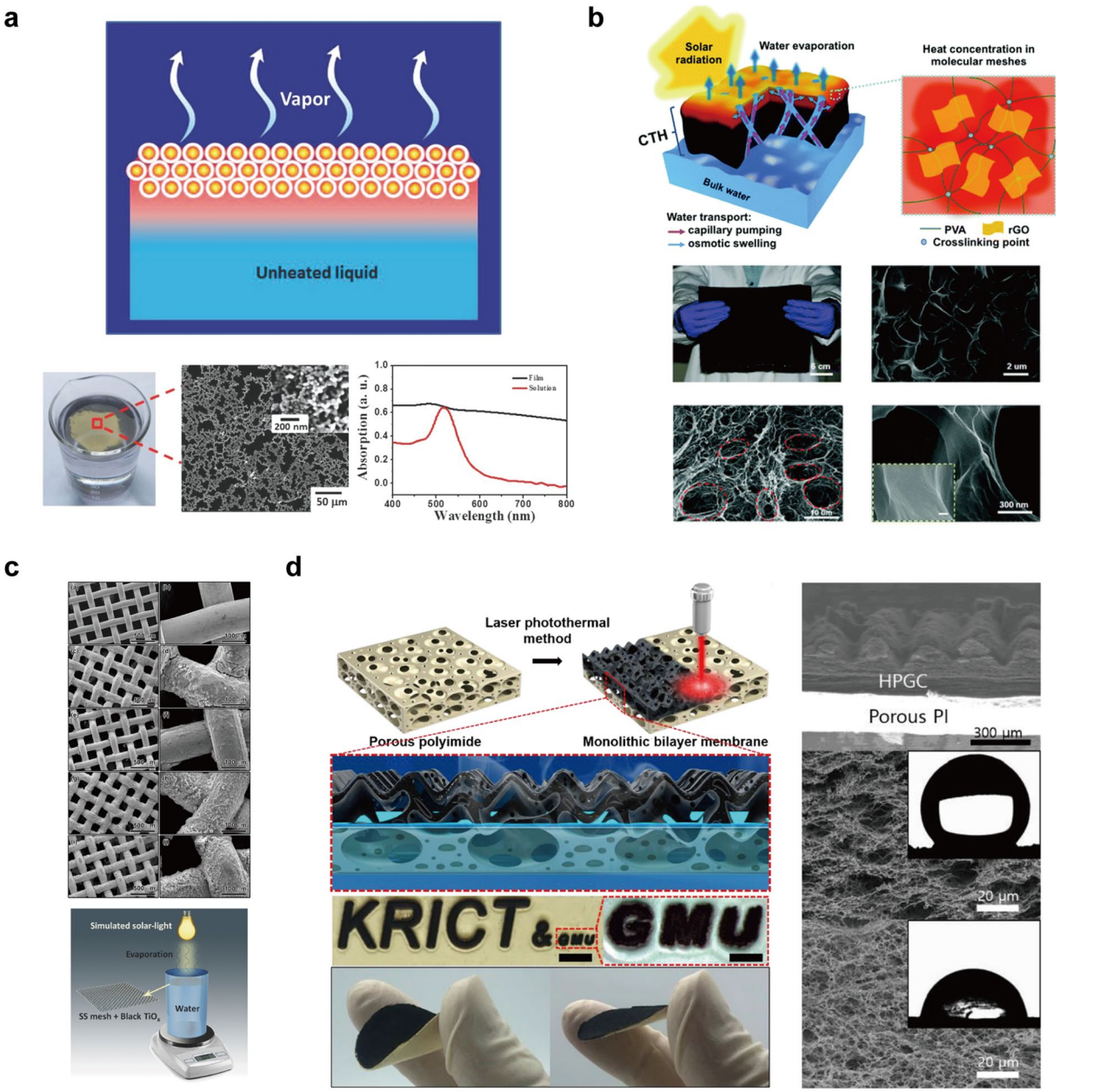

Fig. 6 **a** Schematic illustration of interfacial solar evaporator with floating plasmonic Au nanoparticles. Adapted with permission [16]. Copyright 2014, John Wiley and Sons. **b** Schematic diagram and structural images of hydrogel-based interfacial solar evaporator. Adapted with permission [69]. Copyright 2018, Royal Society of Chemistry. **c** SEM images and schematic illustration of TiO_x nanoparticles coated solar evaporator. Adapted with permission [26]. Copyright 2017, John Wiley and Sons. **d** Carbon based evaporator fabricated by ablation of porous polyimide foam with a CO_2 laser. Adapted with permission [80]. Copyright 2020, Elsevier

membranes. Floatable structure materials such as paper [75–79], mesh [26], or foams [80–83] were modified to have high absorbance by coating the surface with carbon mixed particles [84–86], graphite mixtures [75, 82, 83], or many other light absorber materials. For example, the surface of stainless-steel mesh was modified by spin-coating titanium dioxide nanoparticles to the surfaces to achieve a high absorbance solar evaporator (Fig. 6c) [26]. Scanning electron microscopy images of the TiO_2 coated stainless-steel mesh with different Mg concentration mixture, which act as a light absorbing agent, are shown in Fig. 6c. The fabricated TiO_x coated stainless steel mesh device demonstrated a high evaporation rate up to 0.80 kg m^{-2} h^{-1} under 1-Sun illumination and showed an energy utilization efficiency of 50.3%. Interfacial solar evaporator based on carbon materials is shown in Fig. 6d [80]. By ablating the

surface of porous polyimide (PI) foam with a CO_2 laser, a photothermally laser-induced graphitic carbon upper layer was fabricated. This hierarchically porous graphitic carbon (HPGC) layer was reported to exhibit ~ 97% absorption at the range of 250–2500 nm and showed an energy utilization efficiency of 83.2%. In addition to the method of reforming the surface with laser, several other deposition strategies were also explored. Coating metals, such as Au [76–79, 87, 88] or Ni [89] on floatable structures has been employed to exhibit plasmonic photothermal conversion. Hybrid evaporators using absorbers such as MoS_2 [90, 92], and Ti_xO_y [27–29] were developed as well.

1D research mainly focused on advances in photothermal conversion. Various light absorbing materials such as metal oxides that can be easily manufactured in large quantities from inexpensive and scalable materials or carbon-based materials have been studied. However, because a 1D system is in contact with the water surface, most of the heat loss cannot be avoided, which is a great disadvantage in heat utilization. Because the photothermal layer are in contact with water either directly or through a thin sheet structure, a strategy was needed to minimize the area in contact with water. Therefore, in the next section, we will introduce systems of higher dimensions that overcome heat loss issues.

5.2 2D Interfacial Solar Evaporators

The difference between 1D and 2D interfacial solar evaporators is that the pores of the porous material in the 2D systems are anisotropic. 2D systems are mostly composed of heterogeneous structures, in which the light absorbing layer converting the solar energy and the layer responsible for water transportation are made of different materials. 2D systems could be broadly distinguished into two types. One is a system in which only the surface of a porous material is converted into a substance that absorbs light efficiently. The other type is a system which has a water transportation layer separate from the absorber layer.

Many studies have utilized the carbonizing process of the surface of a natural wood to use as the absorber layer. The unconverted wood layer below the carbonized layer is used as a water transfer channel using the capillary effect [94–101]. Typical methods for carbonization include coating the surface with carbon nanoparticles, carbon nanotubes or graphene oxide, [94–96] and heating or burning

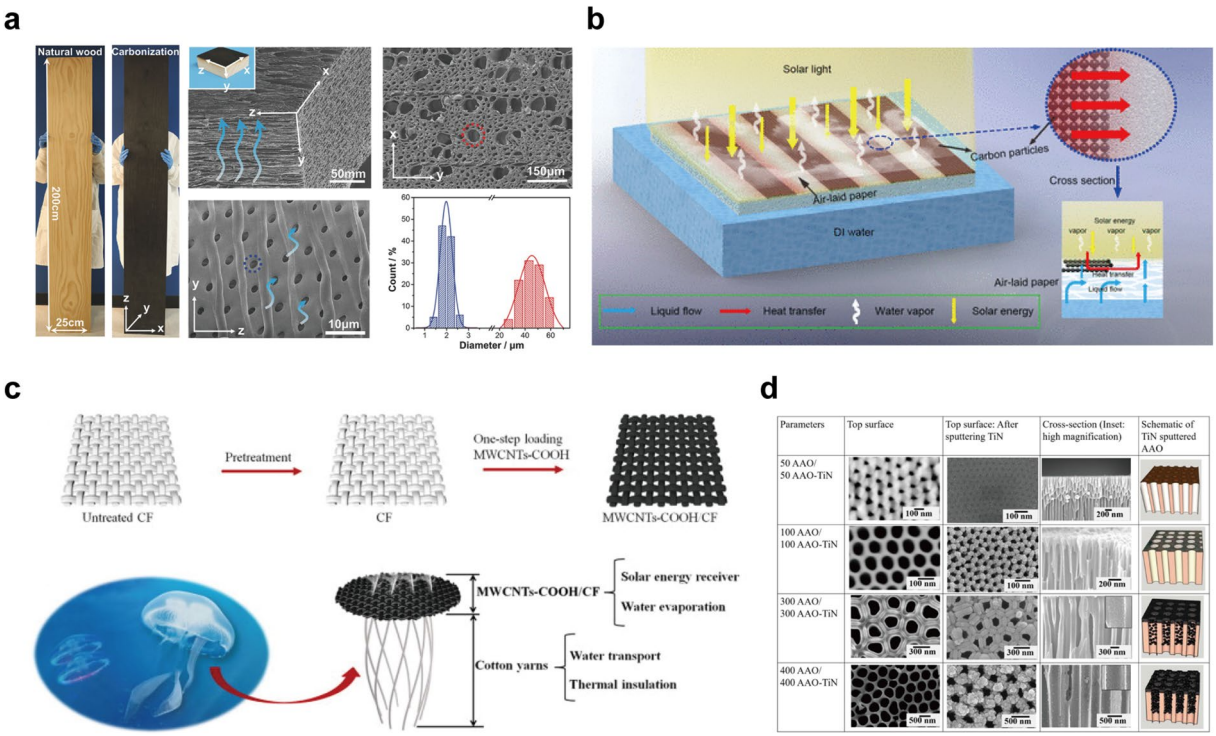

Fig. 7 **a** Wood based efficient interfacial solar evaporator. Adapted with permission [98]. Copyright 2018, John Wiley and Sons **b** Interfacial solar evaporator with patterned carbon black on air-laid paper. Adapted with permission [105]. Copyright 2019, American Chemical Society. **c** Interfacial solar evaporator imitating a jellyfish. Adapted with permission [107]. Copyright 2020, Elsevier. **d** TiN coated on anodic aluminum oxide templates. Adapted with permission [115]. Copyright 2019, John Wiley and Sons

at high temperatures [97–101]. Chen et al. reported a low-cost, scalable solar steam generation system by making natural balsa wood flexible through chemical treatment for portable application and coating the hairy surface with carbon nanotube [95]. Similarly, Liu et al. produced a highly efficient system by applying a graphene oxide (GO) solution

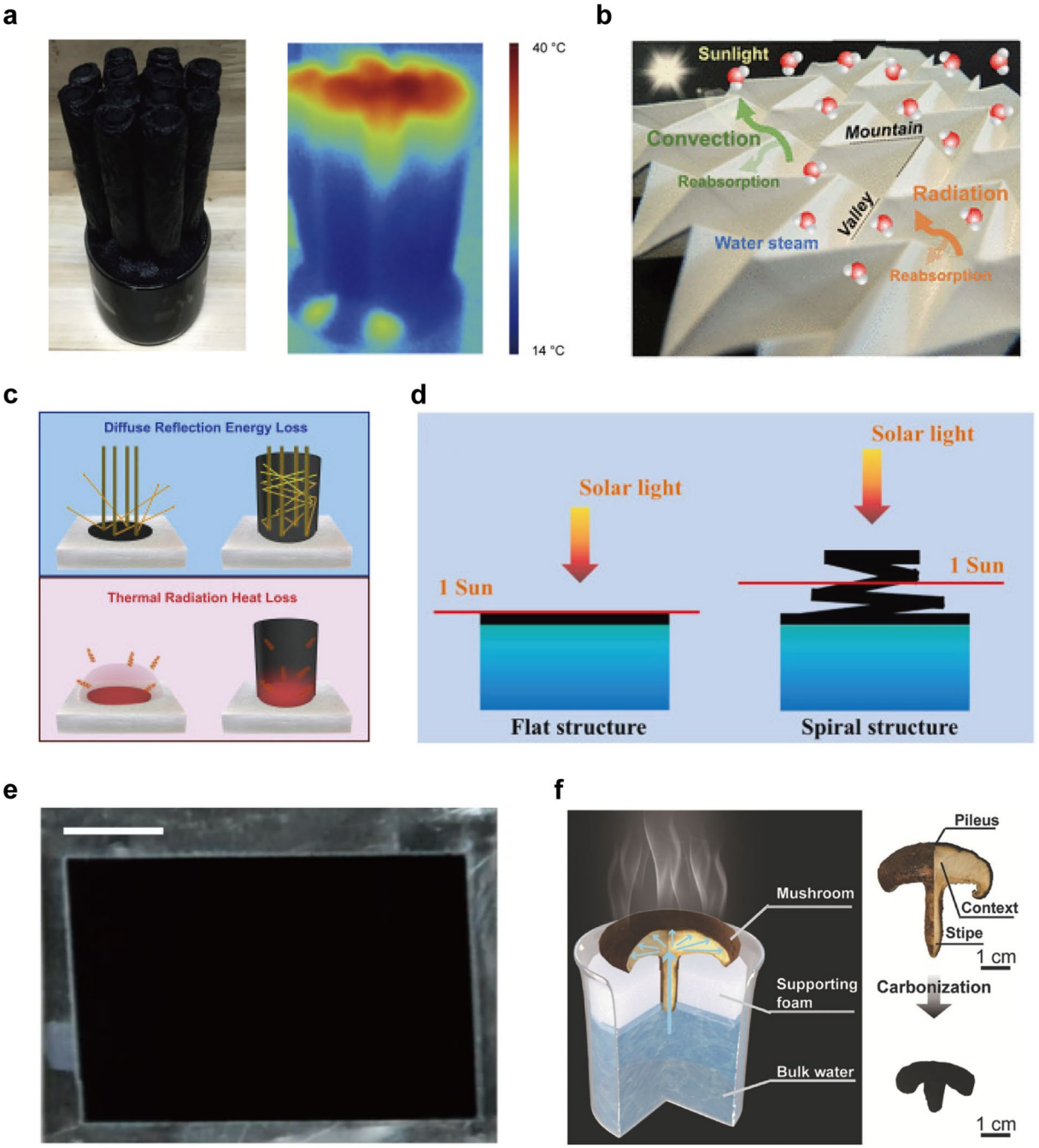

Fig. 8 **a** Rolled cellulose papers with carbon black NPs coating can absorb ambient heat due to its low temperature and fin shape 3D structure. Adapted with permission [48]. Copyright 2018, Elsevier. **b** Origami-based solar interfacial evaporator using Miura-ori tessellation. Adapted with permission [118]. Copyright 2018, American Chemical Society. **c** The hollow cylindrical shape evaporator which can re-absorb light and heat. Adapted with permission [122]. Copyright 2018, Elsevier. **d** Kirigami-based 3D spiral evaporator. Adapted with permission [123]. Copyright 2021, Elsevier. **e** Panel-shape evaporator with bifaciality. Adapted with permission [49]. Copyright 2020, Springer Nature. **f** Carbonized mushroom as efficient interfacial solar evaporators. Adapted with permission [125]. Copyright 2017, John Wiley and Sons

on radially cut basswood [96]. The solution was naturally dried to form the absorbing layer and achieved nearly a 7 times higher mass change of water compared with pure wood under a 12-Sun illumination [96]. Water transportation is mostly carried out using a channel opened in the direction of the wood growth, but a case of transporting water through pits connecting the wood channel has been also reported. Liu et al. reported a higher evaporation rate up to 12.26 kg m^{-2} h^{-1} under 10-Sun illumination through improved heat localization by carbonizing the surface of the wood in the direction perpendicular to the wood channel [98]. The longitudinal channels were found to serve as an excellent thermal barrier between the absorber layer and the water transport layer (Fig. 7a).

The systems utilizing different materials for the absorber layer and the transport layer can be roughly divided into two branches. One is a method that transports water to the light absorbing layer by bypassing through a thermal insulator placed between the layers [17, 102–106]. In previous studies concerning bypass transportation, supporting layers were usually paper [102–105], membrane filter [17] or wood [106], and the insulators were mainly expanded polystyrene (EPS) layers [17, 102–105] or expanded polyethylene (EPE) foam [106]. Luo et al. coated air-laid paper with carbon black and used it as a light absorbing layer. Rather than coating the entire area of the absorber layer, it was possible to reduce the cost by patterning the surface which resulted in increased heat and mass transfer rate in the horizontal direction of the absorber layer (Fig. 7b) [105]. On the other hand, there are cases in which the supporting layer itself has provided both excellent thermal insulation and water transportation [30, 36, 107–116]. Systems were developed using more diverse materials in place of bypass routes for the supporting layer, such as cotton [107], nanofibrillated cellulose [108], paper [109], graphene [110, 111], metal foam [30], wood [113, 116] and nanoporous material [36, 112, 114, 115]. In interfacial solar evaporator-related studies, there are quite a few cases where the system is constructed following the shape of the natural species. Among them, Qi et al. reported a significantly improved results by making a system in the form of a jellyfish (Fig. 7c) [107]. The light absorbing layer was fabricated by loading carboxylated multi-walled carbon nanotubes to cotton fiber, imitating a body part of the jellyfish. Moreover, they used cotton yarns, which resemble the tentacles of jellyfish, to serve as an effective transport layer and insulator. In the case of utilizing nanoporous template as a supporting layer, Kaur et al. developed a system by sputtering TiN to anodic aluminum oxide (AAO) templates with various pore sizes and reported a high steam generation efficiency of 92% at a 1-Sun condition (Fig. 7d) [115].

Even with materials similar to that of the 1D systems, 2D solar evaporators with high efficiency over 90% were attained by minimizing heat loss while maintaining a continuous water supply through anisotropic pore structure. In addition, high-efficiency and scalable systems were achieved through novel processes or materials such as carbonization. However, there is a fundamental limitation that cannot exceed the maximum energy supply of solar power (1000 W m^{-2}). In the next section, we will introduce studies that have exceeded this limit through re-absorption of light or absorption of ambient heat.

5.3 3D Interfacial Solar Evaporators

The 3D interfacial solar evaporator systems use a structure perpendicular to the water surface or suspended above bulk water tipping a certain edge of its system, while a planar system (1–2D) fully faces or is parallel to the water surface. Although the 3D structures have the disadvantage of the capillary flow path being relatively long, it has extraordinary merit such that it can absorb direct and reflected sunlight through a three-dimensional shape. In addition, it also absorbs thermal energy from the surroundings, exhibiting an efficiency exceeding 100%. Non-planar, 3D macrostructures such as a fin, hollow cone, arch, and panel shape were introduced by using various manufacturing methods.

A cylindrical fin shape was rendered by rolling cellulose paper coated with carbon black NPs [48]. The evaporation rate of this device exceeded the theoretical efficiency at 1000 W m^{-2} (1 Sun), because it additionally absorbs the ambient heat in the lower region, which is cooler than the ambient temperature, as can be seen in the thermal image (Fig. 8a). To render the vertically ordered pillar structures [117], a pillar array structure was formed by freeze drying graphene oxide suspension, and then converting it to reduced GO by laser light.

Origami and Kirigami are papercraft techniques of folding or cutting paper. These techniques are useful for constructing 3D structures from 2D planar materials. Due to these characteristics, many studies applied origami [118–120] and kirigami [121–123] for sheet-based solar evaporators. 3D structures created by origami have demonstrated their merit by re-absorbing radiative and convective loss due to their complex geometry. Based on Miura-ori tessellation solar evaporators achieved over 100% efficiency by trapping reflected light and heat loss in the folded structures with repeated mountains and valleys (Fig. 8b) [118]. Additionally, rose-like 3D origami interfacial solar evaporators [119] have demonstrated considerable evaporation rate improvements up to 2.12 kg m^{-2} h^{-1}. These folded paper structures present near 100% absorption as the number of folding increases. In addition, a transformable 2D–3D hybrid system was developed for adaptation to diverse weather conditions [120].

The light trapping shape such as a hollow cone or cylinder can be easily fabricated by kirigami [121–123]. A 3D

Table 1 Summary of studies on interfacial solar evaporators

Structure dimension											
1D				2D				3D			
Materials	q_e	η	References	Materials	q_e	η	Reference	Materials	q_e	η	References
Carbonaceous and polymeric materials	1	64	[15]	Carbonaceous and polymeric materials	1.6	74	[94]	Carbonaceous and polymeric materials	1.67	114	[48]
	0.83	52	[70]		0.95	65	[95]		1.59	100	[118]
	1.62	83	[72]		1.50	86	[97]		2.12	91.5	[119]
	1.34	83.5	[80]		1.08	74	[98]		1.47	85.9	[120]
	1.51	97.1	[81]		1.05	72	[99]		1.7	93.8	[121]
	0.9	65	[82]		0.83	57.3	[100]		4.35	185.9	[123]
	1.21	80	[84]		1.04	75.1	[101]		1.5	96	[124]
	1.15	80	[86]		1.28	88	[103]		2.1	95	[117]
Plasmonic metal nanoparticles	2.5	87.4	[69]		1.46	91.7	[104]		1.48	78	[125]
	0.67	46	[79]		1.17	85.2	[107]		3.13	132	[126]
	1.33	91	[88]		1.45	80	[17]		1.33	90	[127]
	1.41	94	[89]		1.25	85.6	[108]		2.02	75	[128]
	1.03	65.2	[56]		1.44	89.7	[109]		2.38	149.6	[129]
Metal oxide-based semiconductors	1.13	70.9	[25]		1.27	87.5	[110]		1.95	116	[130]
	0.80	50.3	[26]		1.5	80	[111]	Metal oxide-based semiconductors	2.04	100.8	[122]
	1.3	80.1	[92]		1.45	91.3	[106]		1.96	94.5	[33]
	1.52	94	[28]	Plasmonic metal nanoparticles	0.91	57.6	[112]				
	4	93	[29]		0.93	63.8	[36]				
	1.06	67.7	[93]		0.98	69	[113]				
				Metal oxide-based semiconductors	1.31	79.8	[30]				
					1.28	82.5	[116]				

q_e is the evaporation rate (kg m^{-2} h^{-1}), and η is the efficiency of device (%)

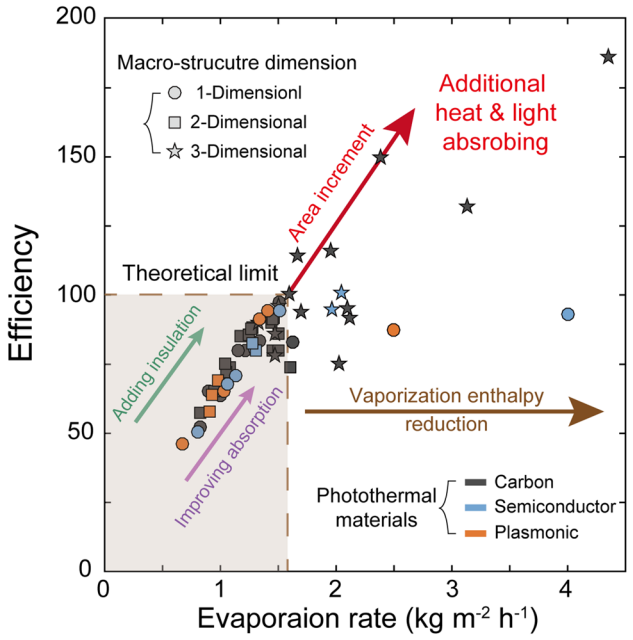

Fig. 9 The comparison of the evaporation rate and the efficiency of recent works on interfacial solar evaporators. The shaded box is enclosed by the theoretical limit under 1-Sun condition. For photothermal materials category, "Carbon", "Semiconductor", and "Plasmonic" means carbonaceous and polymeric materials, metal oxide-based semiconductors, and plasmonic metal nanoparticles, respectively

hollow-structured interfacial solar evaporator can be simply tailored from a photothermal material coated membrane (Fig. 8c). This hollow shape [121, 122] enables additional energy harvesting and provides additional surface area to promote evaporation performance. In addition, a 3D spiral shape, which is transformable to a 2D planar shape, was suggested with a much higher evaporation rate (up to 4.35 kg m^{-2} h^{-1}) (Fig. 8d) [123].

Metal-based 3D interfacial solar evaporators with an arch shape were also introduced to improve the thermal insulation and evaporation performance. A Cu-based evaporator system [33, 124] was built by fabricating a metal framework bent into a bridge shape. Due to the intrinsic superhydrophilicity of metal oxide nanostructures to repel oil, these systems showed high evaporation rate even if on oil contaminated water. Furthermore, the bi-faciality, which is a promising property for photovoltaic application, has been achieved with bi-facial hierarchical structured aluminum metal plate (Fig. 8e) [49]. Moreover, the bi-facial system, with the photothermal layer coated on both sides of the plate can harvest reflected and diffused light by the rear side.

In addition, 3D interfacial solar evaporators derived from a natural material or inspired by the structure of natural organisms were investigated. 3D-shaped devices were developed by simply carbonizing all-natural raw substances (Fig. 8f), such as mushrooms [125], bamboos [126], and lotus [127]. These devices have the advantages to achieve environmentally benign system using eco-friendly materials. In addition, various systems consisting of a stem that raises water to a leaf and leaf-like structure where evaporation occurs have been proposed inspired by the transpiration of plants [128–130].

6 Conclusions

In summary, we reviewed the fundamental physics of interfacial solar evaporators and diverse fabrication methods, categorized by the fluid transport dimension. Highly efficient interfacial solar evaporator can be achieved through the underlying physics involved in light absorption, heat utilization and capillary transport. We introduced the basic principles and types of photothermal materials and the fundamental physics of heat and mass transfer to minimize the heat loss, and to overcome the capillary limitation to supply water under evaporation. We summarized recent works, which used various materials with numerous fabrication methods, sorted by dimensional categories in Table 1. Interfacial solar evaporator research began with the development of high efficiency photothermal layers on the surface of the water (1D) and converged to a 2D configuration system with an insulating layer and a capillary path that minimizes the water contact to approach 100% efficiency as shown in the shaded area in Fig. 9. In addition, vaporization enthalpy reduction has been introduced to high evaporation rate (> 1.58 kg m^{-2} h^{-1}) under 1-Sun condition (brown arrow in Fig. 9). Furthermore, 3D structured interfacial solar evaporators, which are capable of absorbing reflected or scattered light and ambient heat, have been developed with results that exceeded the theoretical limit of 100% efficiency (red arrow in Fig. 9).

However, there are still challenges to be solved in interfacial solar evaporators. First, the evaporation surface is easily contaminated due to sediments such as salts and organic contaminants generated while evaporating contaminated water. Therefore, additional efforts are required for salt-rejection and antifouling techniques to ensure long-term stability. Second, it is necessary to develop fabrication methods towards large-scale mass production because interfacial solar evaporator still remains at the laboratory scale or as a portable device for one person. Third, vapor collection in the last stage of clean water production is one of the bottlenecks, and it is necessary to find ways to improve the water collection performance. Therefore, to solve the above-mentioned problems, further progress is highly desirable in understanding the developed materials and the fundamental physics.

Acknowledgements This work was supported by the National Research Foundation of Korea (Grant nos. NRF-2020R1C1C1005880 and NRF-2018R1A3B1052541) via SNU-IAMD and SNU Creative-Pioneering Researchers Program via Institute of Engineering Research at SNU.

References

1. Shannon, M. A., Bohn, P. W., Elimelech, M., Georgiadis, J. G., Mariñas, B. J., & Mayes, A. M. (2008). Science and technology for water purification in the coming decades. *Nature, 452*(7185), 301–310.
2. Schewe, J., Heinke, J., Gerten, D., Haddeland, I., Arnell, N. W., Clark, D. B., et al. (2014). Multimodel assessment of water scarcity under climate change. *Proceedings of the National Academy of Sciences of the United States of America, 111*(9), 3245–3250.
3. Dalvi, V. H., Panse, S. V., & Joshi, J. B. (2015). Solar thermal technologies as a bridge from fossil fuels to renewables. *Nature Climate Change, 5*(11), 1007–1013.
4. Lewis, N. S. (2007). Toward cost-effective solar energy use. *Science, 315*(5813), 798–801.
5. Lewis, N. S. (2016). Research opportunities to advance solar energy utilization. *Science, 351*(6271), 1920.
6. Qiblawey, H. M., & Banat, F. (2008). Solar thermal desalination technologies. *Desalination, 220*(1), 633–644.
7. Li, C., Goswami, Y., & Stefanakos, E. (2013). Solar assisted sea water desalination: A review. *Renewable and Sustainable Energy Reviews, 19,* 136–163.
8. Thirugnanasambandam, M., Iniyan, S., & Goic, R. (2010). A review of solar thermal technologies. *Renewable & Sustainable Energy Reviews, 14*(1), 312–322.
9. Kabeel, A. E., & El-Agouz, S. A. (2011). Review of researches and developments on solar stills. *Desalination, 276*(1), 1–12.
10. Rufuss, D. W. D., Iniyan, S., Suganthi, L., & Davies, P. A. (2016). Solar stills: A comprehensive review of designs, performance and material advances. *Renewable and Sustainable Energy Reviews, 63,* 464–496.
11. Hale, G. M., & Querry, M. R. (1973). Optical constants of water in the 200-nm to 200-μm wavelength region. *Applied Optics, 12*(3), 555–563.
12. Neumann, O., Urban, A. S., Day, J., Lal, S., Nordlander, P., & Halas, N. J. (2013). Solar vapor generation enabled by nanoparticles. *ACS Nano, 7*(1), 42–49.
13. Ni, G., Miljkovic, N., Ghasemi, H., Huang, X., Boriskina, S. V., Lin, C.-T., et al. (2015). Volumetric solar heating of nanofluids for direct vapor generation. *Nano Energy, 17,* 290–301.
14. Jin, H., Lin, G., Bai, L., Zeiny, A., & Wen, D. (2016). Steam generation in a nanoparticle-based solar receiver. *Nano Energy, 28,* 397–406.
15. Ghasemi, H., Ni, G., Marconnet, A. M., Loomis, J., Yerci, S., Miljkovic, N., et al. (2014). Solar steam generation by heat localization. *Nature Communications, 5,* 4449.
16. Wang, Z., Liu, Y., Tao, P., Shen, Q., Yi, N., Zhang, F., et al. (2014). Bio-inspired evaporation through plasmonic film of nanoparticles at the air–water interface. *Small (Weinheim an der Bergstrasse, Germany), 10*(16), 3234–3239.
17. Li, X., Xu, W., Tang, M., Zhou, L., Zhu, B., Zhu, S., et al. (2016). Graphene oxide-based efficient and scalable solar desalination under one sun with a confined 2D water path. *Proceedings of the National Academy of Sciences of the United States of America, 113*(49), 13953–13958.
18. Bond, T. C., & Bergstrom, R. W. (2006). Light absorption by carbonaceous particles: An investigative review. *Aerosol Science and Technology, 40*(1), 27–67.
19. Zhou, W., y., Xie, S. s., Qian, S. f., Zhou, T., Zhao, R. a., Wang, G., , et al. (1996). Optical absorption spectra of C70 thin films. *Journal of Applied Physics, 80*(1), 459–463.
20. Zhang, L., Tang, B., Wu, J., Li, R., & Wang, P. (2015). Hydrophobic light-to-heat conversion membranes with self-healing ability for interfacial solar heating. *Advanced Materials, 27*(33), 4889–4894.
21. Li, C., Jiang, D., Huo, B., Ding, M., Huang, C., Jia, D., et al. (2019). Scalable and robust bilayer polymer foams for highly efficient and stable solar desalination. *Nano Energy, 60,* 841–849.
22. Jiang, Q., Gholami Derami, H., Ghim, D., Cao, S., Jun, Y.-S., & Singamaneni, S. (2017). Polydopamine-filled bacterial nanocellulose as a biodegradable interfacial photothermal evaporator for highly efficient solar steam generation. *Journal of Materials Chemistry A, 5*(35), 18397–18402.
23. Meyer, J. R., Bartoli, F. J., & Kruer, M. R. (1980). Optical heating in semiconductors. *Physical Review B, 21*(4), 1559–1568.
24. Umlauff, M., Hoffmann, J., Kalt, H., Langbein, W., Hvam, J. M., Scholl, M., et al. (1998). Direct observation of free-exciton thermalization in quantum-well structures. *Physical Review B, 57*(3), 1390–1393.
25. Zhu, G., Xu, J., Zhao, W., & Huang, F. (2016). Constructing black titania with unique nanocage structure for solar desalination. *ACS Applied Materials & Interfaces, 8*(46), 31716–31721.
26. Ye, M., Jia, J., Wu, Z., Qian, C., Chen, R., O'Brien, P. G., et al. (2017). Synthesis of black TiOx nanoparticles by Mg reduction of TiO_2 nanocrystals and their application for solar water evaporation. *Advanced Energy Materials, 7*(4), 1601811.
27. Wang, J., Li, Y., Deng, L., Wei, N., Weng, Y., Dong, S., et al. (2017). High-performance photothermal conversion of narrow-bandgap Ti_2O_3 nanoparticles. *Advanced Materials, 29*(3), 1603730.
28. Liu, X., Cheng, H., Guo, Z., Zhan, Q., Qian, J., & Wang, X. (2018). Bifunctional, moth-eye-like nanostructured black titania nanocomposites for solar-driven clean water generation. *ACS Applied Materials & Interfaces, 10*(46), 39661–39669.
29. Guo, Y., Zhao, X., Zhao, F., Jiao, Z., Zhou, X., & Yu, G. (2020). Tailoring surface wetting states for ultrafast solar-driven water evaporation. *Energy & Environmental Science, 13*(7), 2087–2095.
30. Xu, N., Li, J., Wang, Y., Fang, C., Li, X., Wang, Y., et al. (2019). A water lily-inspired hierarchical design for stable and efficient solar evaporation of high-salinity brine. *Science Advances, 5*(7), 7013.
31. Zhang, C., Yan, C., Xue, Z., Yu, W., Xie, Y., & Wang, T. (2016). Shape-controlled synthesis of high-quality Cu_7S_4 nanocrystals for efficient light-induced water evaporation. *Small (Weinheim an der Bergstrasse, Germany), 12*(38), 5320–5328.
32. Yu, F., Guo, Z., Xu, Y., Chen, Z., Irshad, M. S., Qian, J., et al. (2020). Biomass-derived bilayer solar evaporator with enhanced energy utilization for high-efficiency water generation. *ACS Applied Materials & Interfaces, 12*(51), 57155–57164.
33. Huang, W., Su, P., Cao, Y., Li, C., Chen, D., Tian, X., et al. (2020). Three-dimensional hierarchical Cu_xS-based evaporator for high-efficiency multifunctional solar distillation. *Nano Energy, 69,* 104465.
34. Ding, D., Huang, W., Song, C., Yan, M., Guo, C., & Liu, S. (2017). Non-stoichiometric MoO_3−x quantum dots as a light-harvesting material for interfacial water evaporation. *Chemical Communications, 53*(50), 6744–6747.

35. Pelton, M., Aizpurua, J., & Bryant, G. (2008). Metal-nanoparticle plasmonics. *Laser & Photonics Reviews, 2*(3), 136–159.
36. Zhou, L., Tan, Y., Ji, D., Zhu, B., Zhang, P., Xu, J., et al. (2016). Self-assembly of highly efficient, broadband plasmonic absorbers for solar steam generation. *Science Advances, 2*(4), e1501227.
37. Sáenz, P. J., Wray, A. W., Che, Z., Matar, O. K., Valluri, P., Kim, J., et al. (2017). Dynamics and universal scaling law in geometrically-controlled sessile drop evaporation. *Nature Communications, 8,* 14783.
38. Reid, R. C., Prausnitz, J. M., & Poling, B. E. (1987). *The properties of gases and liquids*. McGraw Hill.
39. Weinbaum, S. (1964). Natural convection in a horizontal circular cylinder. *Journal of Fluid Mechanics, 18*(3), 409–437.
40. Howard, L. N. (1963). Heat transport by turbulent convection. *Journal of Fluid Mechanics, 17*(3), 405–432.
41. Lloyd, J. R., Sparrow, E. M., & Eckert, E. R. G. (1972). Laminar, transition and turbulent natural convection adjacent to inclined and vertical surfaces. *International Journal of Heat and Mass Transfer, 15*(3), 457–473.
42. Fujii, T., & Imura, H. (1972). Natural-convection heat transfer from a plate with arbitrary inclination. *International Journal of Heat and Mass Transfer, 15*(4), 755–767.
43. Kaya, A., Aydın, O., & Dincer, I. (2006). Numerical modeling of heat and mass transfer during forced convection drying of rectangular moist objects. *International Journal of Heat and Mass Transfer, 49*(17), 3094–3103.
44. Goldstein, R. J., Sparrow, E. M., & Jones, D. C. (1973). Natural convection mass transfer adjacent to horizontal plates. *International Journal of Heat and Mass Transfer, 16*(5), 1025–1035.
45. Bowen, I. S. (1926). The ratio of heat losses by conduction and by evaporation from any water surface. *Physical Review, 27*(6), 779–787.
46. Elango, C., Gunasekaran, N., & Sampathkumar, K. (2015). Thermal models of solar still: A comprehensive review. *Renewable and Sustainable Energy Reviews, 47,* 856–911.
47. Yu, Z., Cheng, S., Li, C., Li, L., & Yang, J. (2019). Highly efficient solar vapor generator enabled by a 3D hierarchical structure constructed with hydrophilic carbon felt for desalination and wastewater treatment. *ACS Applied Materials & Interfaces, 11*(35), 32038–32045.
48. Li, X., Li, J., Lu, J., Xu, N., Chen, C., Min, X., et al. (2018). Enhancement of interfacial solar vapor generation by environmental energy. *Joule, 2*(7), 1331–1338.
49. Singh, S. C., ElKabbash, M., Li, Z., Li, X., Regmi, B., Madsen, M., et al. (2020). Solar-trackable super-wicking black metal panel for photothermal water sanitation. *Nature Sustainability, 3*(11), 938–946.
50. Miyazaki, M., Fujii, A., Ebata, T., & Mikami, N. (2004). Infrared spectroscopic evidence for protonated water clusters forming nanoscale cages. *Science, 304*(5674), 1134–1137.
51. Fujii, A., & Mizuse, K. (2013). Infrared spectroscopic studies on hydrogen-bonded water networks in gas phase clusters. *International Reviews in Physical Chemistry, 32*(2), 266–307.
52. Zhao, Y., Zhao, K., Yin, J., Yang, J., Xu, J., Gu, Y., et al. (2019). A nanopump for low-temperature and efficient solar water evaporation. *Journal of Materials Chemistry A, 7*(42), 24311–24319.
53. Guan, Q.-F., Han, Z.-M., Ling, Z.-C., Yang, H.-B., & Yu, S.-H. (2020). Sustainable wood-based hierarchical solar steam generator: A biomimetic design with reduced vaporization enthalpy of water. *Nano Letters, 20*(8), 5699–5704.
54. Zhao, F., Zhou, X., Shi, Y., Qian, X., Alexander, M., Zhao, X., et al. (2018). Highly efficient solar vapour generation via hierarchically nanostructured gels. *Nature Nanotechnology, 13*(6), 489–495.
55. Zhou, X., Zhao, F., Guo, Y., Rosenberger, B., & Yu, G. (2019). Architecting highly hydratable polymer networks to tune the water state for solar water purification. *Science Advances, 5*(6), 5484.
56. Ni, G., Li, G., Boriskina, S. V., Li, H., Yang, W., Zhang, T., et al. (2016). Steam generation under one sun enabled by a floating structure with thermal concentration. *Nature Energy, 1*(9), 16126.
57. Kobus, C. J., & Wedekind, G. L. (2001). An experimental investigation into natural convection heat transfer from horizontal isothermal circular disks. *International Journal of Heat and Mass Transfer, 44*(17), 3381–3384.
58. Al-Arabi, M., & El-Riedy, M. K. (1976). Natural convection heat transfer from isothermal horizontal plates of different shapes. *International Journal of Heat and Mass Transfer, 19*(12), 1399–1404.
59. Globe, S., & Dropkin, D. (1959). Natural-convection heat transfer in liquids confined by two horizontal plates and heated from below. *Journal of Heat Transfer, 81*(1), 24–28.
60. Bauer, T. H. (1993). A general analytical approach toward the thermal conductivity of porous media. *International Journal of Heat and Mass Transfer, 36*(17), 4181–4191.
61. Rayleigh, L. (1892). LVI. On the influence of obstacles arranged in rectangular order upon the properties of a medium. *The London, Edinburgh, and Dublin Philosophical Magazine and Journal of Science, 34*(211), 481–502.
62. Wang, X., Zhai, Z., Chen, Y., & Jiang, H. (2018). A facile, robust and versatile finite element implementation to study the time-dependent behaviors of responsive gels. *Extreme Mechanics Letters, 22,* 89–97.
63. Tang, N., Peng, Z., Guo, R., An, M., Chen, X., Li, X., et al. (2017). Thermal transport in soft PAAm hydrogels. *Polymers, 9*(12), 688.
64. Hassani, A. V., & Hollands, K. G. T. (1987). A simplified method for estimating natural convection heat transfer from bodies of arbitrary shape. In *Proceedings of the 24th National Heat Transfer Conference* (p. 12).
65. Welty, J., Rorrer, G. L., & Foster, D. G. (2020). *Fundamentals of momentum, heat, and mass transfer*. Wiley.
66. Zeng, Y., Yao, J., Horri, B. A., Wang, K., Wu, Y., Li, D., et al. (2011). Solar evaporation enhancement using floating light-absorbing magnetic particles. *Energy & Environmental Science, 4*(10), 4074–4078.
67. Zeng, Y., Wang, K., Yao, J., & Wang, H. (2014). Hollow carbon beads for significant water evaporation enhancement. *Chemical Engineering Science, 116,* 704–709.
68. Chen, R., Wu, Z., Zhang, T., Yu, T., & Ye, M. (2017). Magnetically recyclable self-assembled thin films for highly efficient water evaporation by interfacial solar heating. *RSC Advances, 7*(32), 19849–19855.
69. Zhou, X., Zhao, F., Guo, Y., Zhang, Y., & Yu, G. (2018). A hydrogel-based antifouling solar evaporator for highly efficient water desalination. *Energy & Environmental Science, 11*(8), 1985–1992.
70. Ma, S., Chiu, C. P., Zhu, Y., Tang, C. Y., Long, H., Qarony, W., et al. (2017). Recycled waste black polyurethane sponges for solar vapor generation and distillation. *Applied Energy, 206,* 63–69.
71. Lu, Y., Dai, T., Fan, D., Min, H., Ding, S., & Yang, X. (2020). Turning trash into treasure: Pencil waste-derived materials for solar-powered water evaporation. *Energy Technology, 8*(10), 2000567.
72. Hu, X., Xu, W., Zhou, L., Tan, Y., Wang, Y., Zhu, S., et al. (2017). Tailoring graphene oxide-based aerogels for efficient solar steam generation under one sun. *Advanced Materials, 29*(5), 1604031.

73. Lin, X., Chen, J., Yuan, Z., Yang, M., Chen, G., Yu, D., et al. (2018). Integrative solar absorbers for highly efficient solar steam generation. *Journal of Materials Chemistry A, 6*(11), 4642–4648.
74. Hua, Z., Li, B., Li, L., Yin, X., Chen, K., & Wang, W. (2017). Designing a novel photothermal material of hierarchical microstructured copper phosphate for solar evaporation enhancement. *The Journal of Physical Chemistry C, 121*(1), 60–69.
75. Lou, J., Liu, Y., Wang, Z., Zhao, D., Song, C., Wu, J., et al. (2016). Bioinspired multifunctional paper-based rGO composites for solar-driven clean water generation. *ACS Applied Materials & Interfaces, 8*(23), 14628–14636.
76. Chang, C., Yang, C., Liu, Y., Tao, P., Song, C., Shang, W., et al. (2016). Efficient solar-thermal energy harvest driven by interfacial plasmonic heating-assisted evaporation. *ACS Applied Materials & Interfaces, 8*(35), 23412–23418.
77. Liu, Y., Yu, S., Feng, R., Bernard, A., Liu, Y., Zhang, Y., et al. (2015). A bioinspired, reusable, paper-based system for high-performance large-scale evaporation. *Advanced Materials, 27*(17), 2768–2774.
78. Wang, X., He, Y., Liu, X., Cheng, G., & Zhu, J. (2017). Solar steam generation through bio-inspired interface heating of broadband-absorbing plasmonic membranes. *Applied Energy, 195,* 414–425.
79. Bae, K., Kang, G., Cho, S. K., Park, W., Kim, K., & Padilla, W. J. (2015). Flexible thin-film black gold membranes with ultrabroadband plasmonic nanofocusing for efficient solar vapour generation. *Nature Communications, 6,* 10103.
80. Kim, M., Yang, K., Kim, Y. S., Won, J. C., Kang, P., Kim, Y. H., et al. (2020). Laser-induced photothermal generation of flexible and salt-resistant monolithic bilayer membranes for efficient solar desalination. *Carbon, 164,* 349–356.
81. Han, D.-D., Chen, Z.-D., Li, J.-C., Mao, J.-W., Jiao, Z.-Z., Wang, W., et al. (2020). Airflow enhanced solar evaporation based on Janus graphene membranes with stable interfacial floatability. *ACS Applied Materials & Interfaces, 12*(22), 25435–25443.
82. Wang, G., Fu, Y., Guo, A., Mei, T., Wang, J., Li, J., et al. (2017). Reduced graphene oxide–polyurethane nanocomposite foam as a reusable photoreceiver for efficient solar steam generation. *Chemistry of Materials, 29*(13), 5629–5635.
83. Liu, X., Hou, B., Wang, G., Cui, Z., Zhu, X., & Wang, X. (2018). Black titania/graphene oxide nanocomposite films with excellent photothermal property for solar steam generation. *Journal of Materials Research, 33*(6), 674–684.
84. Li, J., Du, M., Lv, G., Zhou, L., Li, X., Bertoluzzi, L., et al. (2018). Interfacial solar steam generation enables fast-responsive, energy-efficient, and low-cost off-grid sterilization. *Advanced Materials, 30*(49), 1805159.
85. Liu, Y., Chen, J., Guo, D., Cao, M., & Jiang, L. (2015). Floatable, self-cleaning, and carbon-black-based superhydrophobic gauze for the solar evaporation enhancement at the air–water interface. *ACS Applied Materials & Interfaces, 7*(24), 13645–13652.
86. Li, T., Liu, H., Zhao, X., Chen, G., Dai, J., Pastel, G., et al. (2018). Scalable and highly efficient mesoporous wood-based solar steam generation device: Localized heat, rapid water transport. *Advanced Functional Materials, 28*(16), 1707134.
87. Zhang, Z., Wang, Y., Stensby Hansen, P. A., Du, K., Gustavsen, K. R., Liu, G., et al. (2019). Black silicon with order-disordered structures for enhanced light trapping and photothermic conversion. *Nano Energy, 65,* 103992.
88. Kim, J. U., Kang, S. J., Lee, S., Ok, J., Kim, Y., Roh, S. H., et al. (2020). Omnidirectional, broadband light absorption in a hierarchical nanoturf membrane for an advanced solar-vapor generator. *Advanced Functional Materials, 30*(50), 2003862.
89. Wu, D., Qu, D., Jiang, W., Chen, G., An, L., Zhuang, C., et al. (2019). Self-floating nanostructured Ni–NiO_x/Ni foam for solar thermal water evaporation. *Journal of Materials Chemistry A, 7*(14), 8485–8490.
90. Ghim, D., Jiang, Q., Cao, S., Singamaneni, S., & Jun, Y.-S. (2018). Mechanically interlocked 1T/2H phases of MoS_2 nanosheets for solar thermal water purification. *Nano Energy, 53,* 949–957.
91. Hu, H., Wang, Z., Ye, Q., He, J., Nie, X., He, G., et al. (2016). Substrateless welding of self-assembled silver nanowires at air/water interface. *ACS Applied Materials & Interfaces, 8*(31), 20483–20490.
92. Guo, Z., Wang, G., Ming, X., Mei, T., Wang, J., Li, J., et al. (2018). PEGylated self-growth MoS_2 on a cotton cloth substrate for high-efficiency solar energy utilization. *ACS Applied Materials & Interfaces, 10*(29), 24583–24589.
93. Liu, H., Chen, C., Wen, H., Guo, R., Williams, N. A., Wang, B., et al. (2018). Narrow bandgap semiconductor decorated wood membrane for high-efficiency solar-assisted water purification. *Journal of Materials Chemistry A, 6*(39), 18839–18846.
94. Zhang, X.-F., Wang, Z., Song, L., Feng, Y., & Yao, J. (2020). Chinese ink enabled wood evaporator for continuous water desalination. *Desalination, 496,* 114727.
95. Chen, C., Li, Y., Song, J., Yang, Z., Kuang, Y., Hitz, E., et al. (2017). Highly flexible and efficient solar steam generation device. *Advanced Materials, 29*(30), 1701756.
96. Liu, K.-K., Jiang, Q., Tadepallifit, S., Raliya, R., Biswas, P., Naik, R. R., et al. (2017). Wood graphene oxide composite for highly efficient solar steam generation and desalination. *ACS Applied Materials & Interfaces, 9*(8), 7675–7681.
97. Zhang, H., Li, L., Jiang, B., Zhang, Q., Ma, J., Tang, D., et al. (2020). Highly thermally insulated and superhydrophilic corn straw for efficient solar vapor generation. *ACS Applied Materials & Interfaces, 12*(14), 16503–16511.
98. Liu, H., Chen, C., Chen, G., Kuang, Y., Zhao, X., Song, J., et al. (2018). High-performance solar steam device with layered channels: Artificial tree with a reversed design. *Advanced Energy Materials, 8*(8), 89.
99. Xue, G., Liu, K., Chen, Q., Yang, P., Li, J., Ding, T., et al. (2017). Robust and low-cost flame-treated wood for high-performance solar steam generation. *ACS Applied Materials & Interfaces, 9*(17), 15052–15057.
100. Zhu, M., Li, Y., Chen, G., Jiang, F., Yang, Z., Luo, X., et al. (2017). Tree-inspired design for high-efficiency water extraction. *Advanced Materials, 29*(44), 1704107.
101. Kuang, Y., Chen, C., He, S., Hitz, E. M., Wang, Y., Gan, W., et al. (2019). A high-performance self-regenerating solar evaporator for continuous water desalination. *Advanced Materials, 31*(23), 1900498.
102. Song, H., Liu, Y., Liu, Z., Singer, M. H., Li, C., Cheney, A. R., et al. (2018). Cold vapor generation beyond the input solar energy limit. *Advanced Science, 5*(8), 1800222.
103. Liu, Z., Song, H., Ji, D., Li, C., Cheney, A., Liu, Y., et al. (2017). Extremely cost-effective and efficient solar vapor generation under nonconcentrated illumination using thermally isolated black paper. *Global Challenges, 1*(2), 1600003.
104. Wang, X., Gan, Q., Chen, R., Peng, H., Zhang, T., & Ye, M. (2020). Water delivery channel design in solar evaporator for efficient and durable water evaporation with salt rejection. *ACS Sustainable Chemistry & Engineering, 8*(21), 7753–7761.
105. Luo, Y., Fu, B., Shen, Q., Hao, W., Xu, J., Min, M., et al. (2019). Patterned surfaces for solar-driven interfacial evaporation. *ACS Applied Materials & Interfaces, 11*(7), 7584–7590.
106. Liu, P.-F., Miao, L., Deng, Z., Zhou, J., Su, H., Sun, L., et al. (2018). A mimetic transpiration system for record high conversion efficiency in solar steam generator under one-sun. *Materials Today Energy, 8,* 166–173.

107. Qi, Q., Wang, Y., Wang, W., Ding, X., & Yu, D. (2020). High-efficiency solar evaporator prepared by one-step carbon nanotubes loading on cotton fabric toward water purification. *Science of The Total Environment, 698,* 134136.
108. Li, Y., Gao, T., Yang, Z., Chen, C., Luo, W., Song, J., et al. (2017). 3D-printed, all-in-one evaporator for high-efficiency solar steam generation under 1 Sun illumination. *Advanced Materials, 29*(26), 1700981.
109. Wang, Z., Ye, Q., Liang, X., Xu, J., Chang, C., Song, C., et al. (2017). Paper-based membranes on silicone floaters for efficient and fast solar-driven interfacial evaporation under one sun. *Journal of Materials Chemistry A, 5*(31), 16359–16368.
110. Li, Y., Gao, T., Yang, Z., Chen, C., Kuang, Y., Song, J., et al. (2017). Graphene oxide-based evaporator with one-dimensional water transport enabling high-efficiency solar desalination. *Nano Energy, 41,* 201–209.
111. Ito, Y., Tanabe, Y., Han, J., Fujita, T., Tanigaki, K., & Chen, M. (2015). Multifunctional porous graphene for high-efficiency steam generation by heat localization. *Advanced Materials, 27*(29), 4302–4307.
112. Zhou, L., Tan, Y., Wang, J., Xu, W., Yuan, Y., Cai, W., et al. (2016). 3D self-assembly of aluminium nanoparticles for plasmon-enhanced solar desalination. *Nature Photonics, 10*(6), 393–398.
113. Zhu, M., Li, Y., Chen, F., Zhu, X., Dai, J., Li, Y., et al. (2018). Plasmonic wood for high-efficiency solar steam generation. *Advanced Energy Materials, 8*(4), 1701028.
114. Wang, X., Hsieh, M. L., Bur, J. A., Lin, S. Y., & Narayanan, S. (2020). Capillary-driven solar-thermal water desalination using a porous selective absorber. *Materials Today Energy, 17,* 100453.
115. Kaur, M., Ishii, S., Shinde, S. L., & Nagao, T. (2019). All-ceramic solar-driven water purifier based on anodized aluminum oxide and plasmonic titanium nitride. *Advanced Sustainable Systems, 3*(2), 1800112.
116. Li, Z., Zheng, M., Wei, N., Lin, Y., Chu, W., Xu, R., et al. (2020). Broadband-absorbing WO_3-x nanorod-decorated wood evaporator for highly efficient solar-driven interfacial steam generation. *Solar Energy Materials and Solar Cells, 205,* 110254.
117. Zhang, P., Liao, Q., Yao, H., Cheng, H., Huang, Y., Yang, C., et al. (2018). Three-dimensional water evaporation on a macroporous vertically aligned graphene pillar array under one sun. *Journal of Materials Chemistry A, 6*(31), 15303–15309.
118. Hong, S., Shi, Y., Li, R., Zhang, C., Jin, Y., & Wang, P. (2018). Nature-inspired, 3D origami solar steam generator toward near full utilization of solar energy. *ACS Applied Materials & Interfaces, 10*(34), 28517–28524.
119. Li, W., Li, Z., Bertelsmann, K., & Fan, D. E. (2019). Portable low-pressure solar steaming-collection unisystem with polypyrrole origamis. *Advanced Materials, 31*(29), 1900720.
120. Ni, F., Xiao, P., Zhang, C., Liang, Y., Gu, J., Zhang, L., et al. (2019). Micro-/macroscopically synergetic control of switchable 2D/3D photothermal water purification enabled by robust, portable, and cost-effective cellulose papers. *ACS Applied Materials & Interfaces, 11*(17), 15498–15506.
121. Wang, Y., Wang, C., Song, X., Huang, M., Megarajan, S. K., Shaukat, S. F., et al. (2018). Improved light-harvesting and thermal management for efficient solar-driven water evaporation using 3D photothermal cones. *Journal of Materials Chemistry A, 6*(21), 9874–9881.
122. Shi, Y., Li, R., Jin, Y., Zhuo, S., Shi, L., Chang, J., et al. (2018). A 3D photothermal structure toward improved energy efficiency in solar steam generation. *Joule, 2*(6), 1171–1186.
123. Wang, Y., Wu, X., Gao, T., Lu, Y., Yang, X., Chen, G. Y., et al. (2021). Same materials, bigger output: A reversibly transformable 2D–3D photothermal evaporator for highly efficient solar steam generation. *Nano Energy, 79,* 105477.
124. Ma, Q. L., Yin, P. F., Zhao, M. T., Luo, Z. Y., Huang, Y., He, Q. Y., et al. (2019). MOF-based hierarchical structures for solar-thermal clean water production. *Advanced Materials, 31*(17), 1808249.
125. Xu, N., Hu, X., Xu, W., Li, X., Zhou, L., Zhu, S., et al. (2017). Mushrooms as efficient solar steam-generation devices. *Advanced Materials, 29*(28), 1606762.
126. Bian, Y., Du, Q., Tang, K., Shen, Y., Hao, L., Zhou, D., et al. (2019). Carbonized bamboos as excellent 3D solar vapor-generation devices. *Advanced Materials Technologies, 4*(4), 1800593.
127. Tian, Y., Yang, H., Wu, S., Yan, J., Cen, K., Luo, T., et al. (2019). Beyond lotus: Plasma nanostructuring enables efficient energy and water conversion and use. *Nano Energy, 66,* 104125.
128. Shao, Y., Tang, J., Li, N., Sun, T., Yang, L., Chen, D., et al. (2020). Designing a bioinspired synthetic tree by unidirectional freezing for simultaneous solar steam generation and salt collection. *EcoMat, 2*(1), e12018.
129. Xiao, P., He, J., Liang, Y., Zhang, C., Gu, J., Zhang, J., et al. (2019). Rationally programmable paper-based artificial trees toward multipath solar-driven water extraction from liquid/solid substrates. *Solar RRL, 3*(7), 1900004.
130. Zhang, Q., Hu, R., Chen, Y., Xiao, X., Zhao, G., Yang, H., et al. (2020). Banyan-inspired hierarchical evaporators for efficient solar photothermal conversion. *Applied Energy, 276,* 115545.

Publisher's Note Springer Nature remains neutral with regard to jurisdictional claims in published maps and institutional affiliations.

Jungtaek Kim received his B.S. degree from Hongik University in mechanical & system design engineering. He is currently a Ph.D. candidate in the Department of Mechanical Engineering at Seoul National University. His research interests include capillary flows and evaporation dynamics.

Jaewoo Hwang received his B.S. degrees from Seoul National University in mechanical engineering and chemical & biological engineering. He is currently in the combined Master's & Doctoral course in the Department of Mechanical Engineering at Seoul National University. His research interest is the application of stimuli-responsive hydrogels in fluid mechanics.

Seongheon Kim received his B.S. and M.S. degrees from Seoul National University in mechanical & aerospace engineering. He is currently a Ph.D. candidate in the Department of Mechanical Engineering at Seoul National University. His research interests include novel materials and devices for renewable energy applications.

Seong Ho Cho received his B.S. degree from Georgia Institute of Technology in Woodruff School of Mechanical Engineering. He is currently a Ph.D. candidate in the Department of Mechanical Engineering at Seoul National University. His research interests include novel materials and devices for renewable energy applications.

Hanseul Choi received her B.S. degree from Seoul National University in mechanical engineering. She is currently in a combined Master's & Doctoral course. Her research interests include novel materials for energy applications.

Ho-Young Kim received his B.S. degree from Seoul National University and M.S. and Ph.D. degrees from MIT all in mechanical engineering. He is now a Professor of the Department of Mechanical Engineering at Seoul National University. His research activities revolve around microfluid mechanics, biomimetics, and soft matter physics.

Yun Seog Lee received his B.S. degree from Seoul National University, M.S. degree from Stanford University, and Ph.D. degree from MIT. He is currently an Assistant Professor of the Department of Mechanical Engineering at Seoul National University. His research interests include novel materials and innovative nano-scale manufacturing technologies for energy conversion and storage devices.